



# Hydrothermal fault zones in the lower oceanic crust: An example from Wadi Gideah, Samail ophiolite, Oman

Barbara Zihlmann<sup>a,\*</sup>, Samuel Müller<sup>b</sup>, Rosalind M. Coggon<sup>a</sup>, Jürgen Koepke<sup>c</sup>, Dieter Garbe-Schönberg<sup>b</sup>, Damon A.H. Teagle<sup>a</sup>

<sup>a</sup> Ocean and Earth Science, National Oceanography Centre Southampton, University of Southampton, Southampton SO14-3ZH, UK

<sup>b</sup> Institut für Geowissenschaften, Christian-Albrechts-Universität zu Kiel, Kiel, Germany

<sup>c</sup> Institut für Mineralogie, Leibniz Universität Hannover, Hannover, Germany

## ARTICLE INFO

### Article history:

Received 25 May 2018

Accepted 9 September 2018

Available online 13 September 2018

### Key words:

Ocean crust  
Layered gabbro  
Hydrothermal alteration  
Mass changes  
Global chemical flux  
Faults  
Oman ophiolite

## ABSTRACT

Hydrothermal circulation is a key process for chemical and isotopic exchange between the solid Earth and oceans, and for the extraction of heat from newly accreted crust at mid-ocean ridges. However, due to a dearth of samples from intact oceanic crust, or continuous sample suites from ophiolites, there remain major shortcomings in our understanding of hydrothermal circulation in the oceanic crust, especially in the lower plutonic crust. In particular, it remains unknown whether fluid recharge and discharge occurs pervasively or if it is mainly channelled within discrete zones such as faults.

Here, we describe a hydrothermally-altered fault zone that crops out in the Wadi Gideah in the layered gabbro section of the Samail ophiolite of Oman. A one metre thick normal fault comprising deformed chlorite ± epidote fault rock with disseminated chalcopyrite and pyrite, offsets gently dipping layered olivine gabbros. The chlorite-rich fault rocks surround strongly altered clasts of layered gabbro, 50 to 80 cm in size. Layered gabbros in the hanging wall and the footwall are partially altered and abundantly veined by epidote, prehnite, laumontite and calcite veins. In the wall rocks, igneous plagioclase ( $An_{82\pm 2\%}$ ) is partially altered towards more albitic compositions ( $An_{75-81}$ ), and chlorite + tremolite partially replaces plagioclase and clinopyroxene. Clinopyroxene is moderately overgrown by Mg-hornblende.

Whole rock mass change calculations show that the chlorite-rich fault rocks are enriched in Fe, Mn,  $H_2O + CO_2$ , Co, Cu, Zn, Ba, and U, but have lost significant amounts of Si, Ca, Na, Cr, Ni, Rb, Sr, Cs, light rare earth elements (LREE), Eu, and Pb. Gabbro clasts within the fault zone as well as altered rock from the immediate hanging wall show enrichments in Na, volatiles, Sr, Ba and U and depletions of Si, Ti, Al, Fe, Mn, Mg, Ca, Cu, Zn, Rb, Cs, LREE, and Pb. Chlorite thermometry suggests a formation temperature of 300–350 °C for the fault rock and based on the Si loss and solubility of silica in hydrothermal fluids the intensity of alteration requires a fluid to rock ratio of up to 900:1. Strontium isotope whole rock data of the fault rock yield  $^{87}Sr/^{86}Sr$  ratios of 0.7043–0.7048, which is considerably more radiogenic than fresh layered gabbro from this locality ( $^{87}Sr/^{86}Sr = 0.7030–0.7033$ ), and similar to black smoker hydrothermal signatures based on epidote, measured from epidote veins in the footwall and elsewhere in the ophiolite ( $^{87}Sr/^{86}Sr = 0.7043–0.7051$ ). Altered gabbro clasts within the fault zone show similar values with  $^{87}Sr/^{86}Sr$  ratios of ~0.7045–0.7050. In contrast, the hanging and footwall gabbros display values only slightly more radiogenic than fresh layered gabbro. The elevated strontium isotope composition of the fault rock and clasts together with the observed secondary mineral assemblages and calculated mass changes strongly supports the intense interaction with seawater-derived up-welling hydrothermal fluids, active during oceanic spreading. Assuming that such a fault zone is globally representative of faulting in the lower crust, an extrapolation of our results from mass change calculations to elemental fluxes, shows a significant contribution to the global hydrothermal budgets of Si, Ti, Fe, Mn, Mg, Ca,  $H_2O$ , Cu, Zn, Sr and Cs.

© 2018 Elsevier B.V. All rights reserved.

## 1. Introduction

Hydrothermal circulation throughout the oceanic crust is a fundamental process resulting in the exchange of chemical elements between the oceans and the solid Earth (Palmer and Edmond, 1989) as well as for extraction of heat from newly formed crust at mid-ocean ridges

\* Corresponding author.

E-mail addresses: [zihlmann.barbara@gmail.com](mailto:zihlmann.barbara@gmail.com) barbara.zihlmann@soton.ac.uk (B. Zihlmann).

(Morton and Sleep, 1985; Sleep, 1991). Shallow hydrothermal fluid flow permeating the upper part of the oceanic crust is widely accepted for playing a vital role in cooling young crust at mid-ocean ridges. However, to date there remain major shortcomings in our understanding of the geometry and intensity of circulating seawater-derived hydrothermal fluids extending into the lower plutonic rocks of the ocean crust. In particular, the effectiveness of hydrothermal circulation in removing latent heat from the crystallizing magmas is not clear. There remain two, now long-standing, end-member conceptual models of how oceanic crust is accreted: The gabbro glacier model (e.g. Henstock et al., 1993; Morgan and Chen, 1993; Quick and Denlinger, 1993) and the sheeted sills model (e.g. Kelemen et al., 1997; MacLeod and Yaouancq, 2000), although hybrid models are also proposed (e.g. Boudier et al., 1996). The gabbro glacier model proposes the cooling of magma exclusively in a shallow melt lens and the formation of the lower crust by subsidence and downward flow of a crystal mush. In contrast, the sheeted sills model requires that substantial hydrothermal heat extraction occurs deep within the plutonic crust to remove latent heat and allow for in-situ crystallization. Thermal models (Chen, 2001; MacLennan et al., 2004; Theissen-Krah et al., 2016) suggest a mix between both end-member models is most likely but the proportion of crust crystallizing in-situ remains unclear. Cooling rate estimates derived from studies of Ca diffusion in olivine in the lower crust of the Samail ophiolite yield contrasting results as to whether the crust was cooled purely conductively or via hydrothermal circulation. Although data presented by Coogan et al. (2002) favours near conductive cooling, VanTongeren et al. (2008) suggest that hydrothermal circulation is likely to have extended to the base of the crust. Near conductive cooling in the upper plutonic section of the East Pacific Rise was also inferred from rate estimates based upon Mg in plagioclase (Faak et al., 2015) and from a combined Mg in plagioclase and Ca in olivine cooling rate study of gabbros from Hess Deep (Faak and Gillis, 2016). However, Mg and REE bulk diffusion between co-existing plagioclase and pyroxene in gabbros from the East Pacific Rise and Hess Deep (Sun and Lissenberg, 2018) and coupled thermal modelling (Hasenclever et al., 2014) strongly support deep hydrothermal circulation. Due to insufficient observations of intact lower ocean crust it is poorly refined whether the circulation and cooling occurs via pervasive fluid flow along grain boundaries and vein networks or is focussed along major structures such as faults. Millimetre-scale amphibole vein networks are common in the lower gabbros of the ocean crust, and formed at near magmatic temperatures (Bosch et al., 2004; Coogan et al., 2007; Manning et al., 2000, 1996; Nicolas et al., 2003) but it is not clear if these features provide sufficient permeability to allow vigorous enough hydrothermal circulation to extract significant heat (Coogan et al., 2007; Manning et al., 2000, 1996). An alternative mechanism is to remove heat from the lower crust via more discrete, widely spaced regions of focussed fluid flow and discontinuous zones that preserve hydrothermal assemblages of high-temperature (~880 °C) to lower greenschist facies (<300 °C) alteration, observed every ~1 km throughout the crust in the Samail ophiolite in Oman. Enhanced cooling rates are indicated in the surrounding crust of such focussed fluid flow zones (Coogan et al., 2006).

Here we present detailed field, petrographic and geochemical observations of a hydrothermal fault zone located within the lower layered gabbro section of the Samail ophiolite in Oman, approximately 6 km below the paleo-seafloor and 1 km above the Moho transition zone (MTZ). We document the characteristics of a hydrothermal system deep in the crust which is so far only known from shallow hydrothermal environments and show that this fault provided a pathway for focussed hydrothermal discharge, giving evidence that hydrothermal activity was effective in mining heat from the plutonic section. Our primary aim of this study is to discuss the nature of the hydrothermal environment and to quantify elemental changes occurring within the fault zone itself and the alteration halo during intense hydrothermal activity. Finally, we provide first estimates on the contribution of such a fault zone to the global chemical cycle.

## 2. Geological overview

### 2.1. The Samail ophiolite

The Samail ophiolite is regarded as the best analogue of fast-spreading oceanic crust preserved on land (e.g. Nicolas et al., 2000), and stretches approximately 550 km in length and 50 km in width along the coast of the Sultanate of Oman and the United Arab Emirates (UAE). The ophiolite is divided into several massifs (Fig. 1) and shows the complete “Penrose” sequence of rock types expected to be formed at a fast spreading mid-ocean ridge, from extrusive lavas, sheeted dikes, gabbros, layered gabbros and cumulate ultramafic rocks through the crust-mantle transition zone into the mantle sequence comprising harzburgite and locally dunite.

The obducted crust was formed in a spreading centre in the Neotethyan ocean during the Late Cretaceous (Searle and Cox, 1999). Late stage intrusive plagiogranitic bodies within the gabbro section yield ages of 97 to 93 Ma (Rioux et al., 2013) and mark the formation age of the crustal rocks within the ophiolite. There remains ongoing debate as to whether the Samail ophiolite formed at a mid-ocean ridge (MOR) in a major ocean basin or some form of supra-subduction zone setting (SSZ; e.g., Alabaster et al., 1982; Boudier and Nicolas, 2007; Warren et al., 2005, 2007). Most evidence points to the partial influence of a subduction zone (e.g. Godard et al., 2003; Goodenough et al., 2014; Koepke et al., 2009; MacLeod et al., 2013). Although not completely absent, there is general consensus that the subduction zone influence is less pronounced in the southern part of the Samail ophiolite. Consequently, the lower crustal rocks exposed in the Wadi Tayin block of the ophiolite are an ideal location to investigate processes that occur during the accretion of the lower crust at fast spreading mid-ocean ridges.

### 2.2. The fault zone outcrop in Wadi Gideah

The studied fault zone is located in Wadi Gideah (22.894 °N, 58.516 °E), about 15 km north of Ibra, in the crustal section of the Wadi Tayin massif. Wadi Gideah is situated to the west of Wadi Qaffah and Wadi Khadir and to the east of Wadi Saq, Wadis where classic structural, petrographic and isotope geochemical observations on accretion of the crustal section of the ophiolite were made (Hopson et al., 1981; Pallister, 1981; Pallister and Knight, 1981), including oxygen- and strontium isotope studies (Gregory and Taylor, 1981; Lanphere et al., 1981). The north to south oriented Gideah valley cuts through a coherent series of lower oceanic crust and upper mantle rocks, exposing lithologies from the Moho transition zone up to the sheeted dike complex (Pallister and Hopson, 1981). Layered gabbros are the primary rock type and are exposed for ~6.5 km along the length of the valley. The magmatic layering of the gabbros dips ~28° to the south indicating a true thickness of ~3km for the layered gabbro series. These rocks are overlain by foliated gabbros and isotropic high-level gabbros. Sheeted dikes are mostly eroded and are only exposed in small hills at the valley entrance and further out towards the Ibra syncline (Fig. 2). The Wadi Gideah area has been extensively sampled, and major rock types are well characterized in terms of their petrographic and geochemical properties (France et al., 2009; Haase et al., 2016; Müller, 2016; Müller et al., 2017), including sulphur isotopes (Oeser et al., 2012).

Throughout the valley, from the layered gabbros up to the sheeted dikes, there are sub-vertical chlorite-rich zones, decimetres to metres-thick. They consist of dark green, weakly foliated, chlorite-rich rocks with the surrounding wall rock gabbros heavily altered for metres or up to tens of metres (Fig. 2a). Field observations indicate that they occur every 1–2 km, either as isolated features or as part of a more extensively altered zone, similar to what has been described as a focussed fluid flow zone by Coogan et al. (2006). The zone investigated here consists of a chlorite-rich rock surrounded by heavily altered wall rock gabbro but in contrast to other observed zones it clearly crops out as a fault,

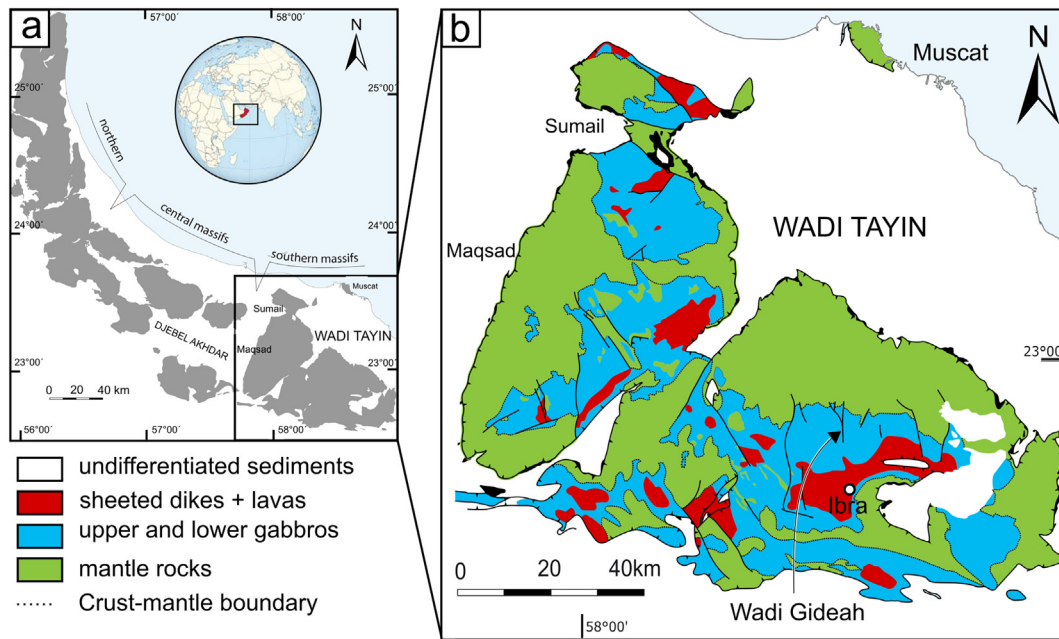


**Fig. 1.** (a) Overview of the Samail ophiolite and (b) Wadi Tayin massif. Wadi Gideah is located approximately 20 km north of the town of Ibra. Map modified after (Nicolas et al., 2000).

making it unique. It is located within the layered gabbro section, approximately 1 km above the Moho transition zone (Fig. 2). A second fault zone is located about 40 m to the east (Fig. 3a). Approximately 500 m towards south-east along strike of this fault zone outcrop, on the southern flank of a small ridge, partially to completely altered, gabbros crop out along the edge of the wadi terrace giving evidence for the continuity of this feature (Fig. 2b).

The fault zone is a normal fault, approximately 1 m wide (Fig. 3b) and crops out over a length of 8 m. Its orientation of  $251/55^\circ$  (dip direction/dip) is sub-orthogonal to the magmatic layering ( $154/38^\circ$ ) nearby and sub-parallel to the mean strike of the sheeted dikes in this area ( $261/71^\circ$ ; Pallister, 1981), although dikes generally dip more steeply. The fault rock consists of a foliated Cu-sulphide-bearing dark greenish to blackish chlorite-rich rock that anastomoses around angular to lenticular clasts (up to 50–80 cm) of altered gabbro. The hanging wall and footwall gabbros are altered and heavily veined by epidote, prehnite, laumontite and carbonate veins for 2.5–3 m. The layered gabbro in the hanging wall is partially altered for ~30 m, manifested in a general bleaching of the rocks (Fig. 3b). A less intense halo extends only about 1 m into the footwall. Representative samples of the fault-rocks, clasts and surrounding altered wall rocks were collected during fieldwork in 2015 and 2016. These samples are compared with relatively fresh layered gabbro samples, collected <500 m distance of the outcrop (Fig. 2b; Mueller et al., 2017).

### 3. Analytical techniques

Polished thin sections were prepared from all samples. Minerals were identified using optical microscopy as well as a Carl Zeiss Leo1450VP Scanning Electron Microscope (SEM), at the University of Southampton, equipped with an Oxford Instruments EDS detector coupled to the Aztec Energy software system. Major element compositions of most minerals were analysed by electron probe microanalysis (EPMA) at the University of Kiel using a JEOL JXA 8900 R EMP operating at 15 kV accelerating voltage and a focused and static 15 nA beam current, applying 15 s counting times. Typical spot sizes were 2  $\mu\text{m}$  except for plagioclase where the beam was defocused to ~5  $\mu\text{m}$ . Compositions of chlorite, epidote and, sulphides in the chlorite-rich fault rock were measured at the Leibniz University in Hannover in Germany using a Cameca SX100 EMPA equipped with five spectrometers and Peak

Sight software with a 15 kV focussed and static beam of 15 nA and 10 s counting times.

Whole rock samples were prepared for geochemical analysis at the University of Southampton. Samples were cut with a diamond saw to remove weathering rinds and prominent mineral veins, and saw marks were ground off with a high-speed diamond grinder. Samples were washed in Milli-Q water and ultrasonicated multiple times and dried at 60 °C overnight. Each sample was crushed into <5 mm chips between a plastic chopping board and sheets of clean paper in a hardened iron fly press, and powdered using a chrome-steel ring mill in a Rocklabs™ bench-top grinder.

Major and trace element (V, Cr, Co, Ni, Cu, Zn, Rb, Sr, Y, Zr, Nb, Cs, Ba, La and Ce) concentrations were analysed by X-ray fluorescence (XRF) using a Spectro XEPOS\_HE Energy Dispersive Polarised X-ray Fluorescence (EDPXRF) Analyser at the University of St. Andrews, following the procedure outlined in Toy et al. (2017). Precision and accuracy were better than  $\pm 2.5\%$  RSD and  $\pm 5\%$  RMSD for major elements and  $\pm 5\%$  RSD,  $\pm 4\%$  RMSD for most trace elements respectively (Table A1). Four samples were analysed at the University of Hamburg, using a PanAnalytical MagixPro X-ray fluorescence spectrometer and following the procedure of Vogel and Kuipers (1987).

Samples for trace element and strontium isotope analysis were processed in a Class 100 Clean Laboratory suite of the Geochemistry Research Group of the University of Southampton. 50 mg of rock powder was dissolved using a standard HF-HNO<sub>3</sub> digestion (for details see Harris et al., 2015). Trace element concentrations were measured by Inductively Coupled Plasma Mass-Spectrometry (ICP-MS) at the University of Southampton using a Thermo X-series II ICP-MS. Precision and accuracy were better than  $\pm 5\%$  RSD and  $\pm 4\%$  RMSD respectively for the majority of the elements (Table A1).

Major and trace elements of four fault zone samples and the eight background gabbros (Table A2) were analysed at Kiel University. For liquid analysis 250 mg of dried powder (105 °C) was dissolved in perfluoroalkoxy (PFA) vials applying a multi-acid digestion protocol. All acids were sub-boiled and, all work was carried out under Class 100 clean laboratory conditions. Procedural blanks, duplicates, and international reference materials were processed the same way (for details see Garbe-Schönberg, 1993). Reproducibility of this digestion procedure is typically better than 1 %RSD (1SD). Major elements were analysed using a Spectro CIROS SOP ICP-OES. SiO<sub>2</sub> cannot be analysed

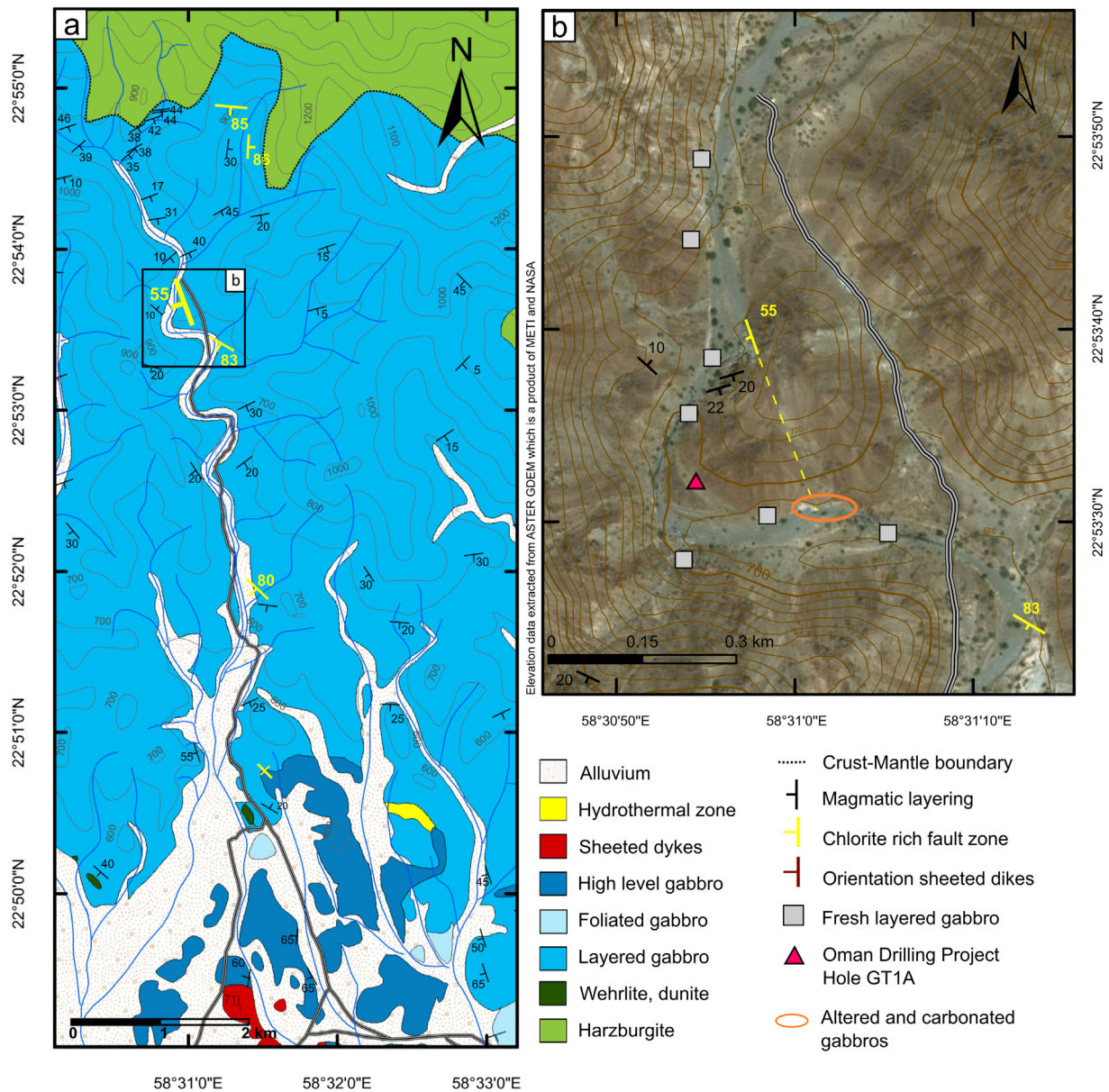


**Fig. 2.** (a) Geological map of Wadi Gideah modified after (Peters et al., 2008). Wadi Gideah cuts through a coherent series of oceanic crustal rock from the Moho transition zone up to the layered gabbros, foliated gabbros, high-level gabbros, and the sheeted dikes. The magmatic layering dips on average 28° S in the upper part of the valley. Approximately sub-orthogonal to the layering and steeply oriented chlorite-rich zones were mapped with a spacing of 1–2 km throughout the whole valley. The chlorite-rich fault zone investigated here is located about 1 km above the Moho. (b) Overview of the area around the chlorite-rich fault zone (displayed in yellow). Locations of fresh layered gabbro samples are shown in light grey squares and the location of the ICDP Oman Drilling Project Hole GT-1A is displayed with a pink triangle.

after digestion procedures including hydrofluoric acid and were therefore calculated to 100% oxides with due regard to loss on ignition. Analytical precision was found to be better than 0.5–1%. Matrix-matched calibration was done by solutions of certified reference materials basalt BHVO-2, basalt BE-N, and granite AC-E processed the same way as the samples. Accuracy was monitored with running digested solutions of basalt BIR-1 and gabbro JGb-2. Minor and trace element mass fractions were determined using an AGILENT 7500cs with (Be, In, Re) internal standardisation. The analytical precision is typically better than 0.5–2% RSD (1SD) for all elements analyzed. Results for reference materials BHVO-2 and JGb-1 are reported in Table A1.

Bulk composition of the aforementioned samples was also determined by LA-ICP-MS after regrinding the samples and pressing into nano-particulate pressed powder pellets (NPP). A 193 nm ArF excimer laser ablation system (GeoLasPro, Coherent) coupled

to an Agilent 7500s ICP-MS was used here. The advantage of this approach is the full recovery of HFSE composition from gabbros containing accessory minerals (zircon, spinel). Details of this procedure can be found in Garbe-Schönberg and Müller (2014). Initial calibration was done against NIST SRM612 using Ca as an internal standard. For applying a matrix-matched correction BHVO-2, BIR-1 and JGb-1 were prepared the same way as the samples and analysed in the same batch. Analytical precision is typically better than 1–5%RSD (1SD) for all elements analysed at concentrations >10× LOD (Table A1).

All samples analysed at the University of Southampton for their strontium isotopic composition were leached with 10% analytical grade acetic acid prior to digestion to remove secondary calcium carbonate. Strontium was separated from dissolved samples using Strontium spec<sup>TM</sup> columns (for details see Harris et al., 2015) and analysed

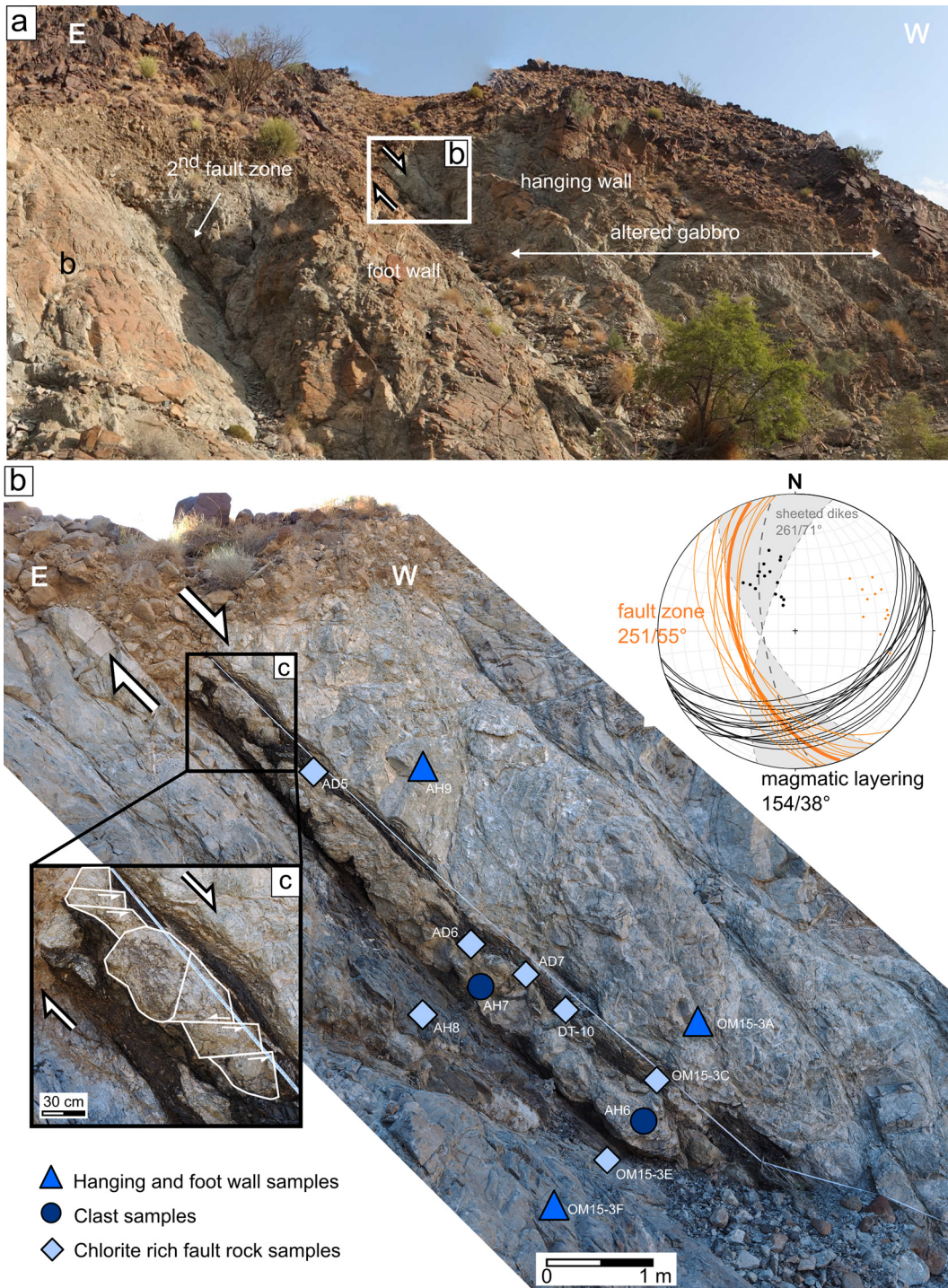


**Fig. 3.** (a) Photo of the fault zone outcrop. Note a second chlorite-rich fault zone is located to the East. Especially in the hanging wall, the gabbros are intensely altered. (b) A detailed overview of the fault zone. Sample locations are marked; chlorite-rich fault zone (light blue diamonds), clasts (dark blue circles), hanging wall and footwall (royal blue triangles). The stereographic projection (dip direction/dip) shows the orientation of the fault zone relative to the orientation of the magmatic layering around the fault zone and the upper part of the valley as well as the orientation of sheeted dikes (Pallister, 1981). (c) Blow-up and sketch of the shear sense indicating a normal fault by top to the left domino-type fracturing of the clasts.

using a ThermoFisher Scientific TritonPlus TIMS. Strontium standard NBS987 was measured as an external standard. Throughout the analytical period the mean value of NBS987 ( $n = 25$ ) was  $^{87}\text{Sr}/^{86}\text{Sr} = 0.710241 \pm 0.000018$  (2SD). Internal precision was monitored by measuring 150 ratios per sample and the error of each measurement is reported as the two standard error (2SE).

Strontium isotope ratios of background gabbros were determined at the Institute of Mineralogy of the Hannover University

following Pin et al. (1994). The analyses were carried out with a ThermoFinnigan Neptune MC-ICP-MS. International standards, used for precision monitoring, were AMES, BIR-1, JGB-2, JMC, and NIST SRM 987.  $^{86}\text{Sr}$  and  $^{87}\text{Sr}$  were corrected for  $^{86}\text{Kr}$  and  $^{87}\text{Rb}$  interferences and  $^{87}\text{Sr}/^{86}\text{Sr}$  corrected for mass fractionation. The mean value for  $^{87}\text{Sr}/^{86}\text{Sr}$  in the external standard NBS987 was  $0.710276 \pm 0.000012$  (2SD). All  $^{87}\text{Sr}/^{86}\text{Sr}$  values were corrected to a NBS987 value of  $^{87}\text{Sr}/^{86}\text{Sr} = 0.710248$ .

## 4. Petrography

### 4.1. Fresh layered gabbro

Eight samples of fresh layered gabbro within 500 m of the fault zone outcrop were taken to provide background reference samples (Table A2). These samples are a subset of a larger suite of rocks focussing on a reference section through the lower oceanic crust of fast-spreading ridges in the Wadi Gideah (Mueller et al., 2017). These olivine-bearing to olivine gabbros are fine to medium grained and consist of about 50% plagioclase, 40% clinopyroxene and 10% olivine. Orthopyroxene is absent. The original magmatic assemblage is mostly preserved although in some rocks hornblende and tremolite/actinolite partially overgrow clinopyroxene. Primary oxides are rare. Igneous plagioclase is partially altered to more albitic compositions. Where clinopyroxenes are in contact with plagioclase, chlorite is developed along some grain boundaries and fractures, commonly with secondary oxides (Fig. 4a, b). Olivine is heavily fractured, serpentinized and partially forms iddingsite, but cores are mostly unaltered. Total alteration is typically less than 5 to 10%.

### 4.2. Footwall and hanging wall

The footwall sample (OM15-3F) is relatively fresh compared to the other fault zone-related samples, showing total alteration of 30–40%. The style of alteration is similar to that in the background gabbros. The formation of chlorite after plagioclase and clinopyroxene as well as actinolite + tremolite after clinopyroxene mostly occurs along grain boundaries. Fresh olivine is rare. Cores of clinopyroxenes are preserved although they are heavily traversed by a dense networks of fractures which is accompanied by secondary oxides and sub-microscopic alteration phases growing into fresh regions thereby attenuating the transparency. Plagioclase shows yellowish to light-brownish shading. A fracture related overprint is also present in plagioclase but this is not as strong as for clinopyroxene (Fig. 4c, d).

The total alteration intensity for the two hanging wall samples (AH9, OM15-3A; Fig. 4e, f) ranges between 50 and 80% with the initial magmatic texture and mineralogy being only partially preserved. Clinopyroxenes have a “rusty” appearance with corroded grain boundaries and abundant fractures and are commonly replaced by sub-micron to micron brown to green hornblende blades and tremolite/

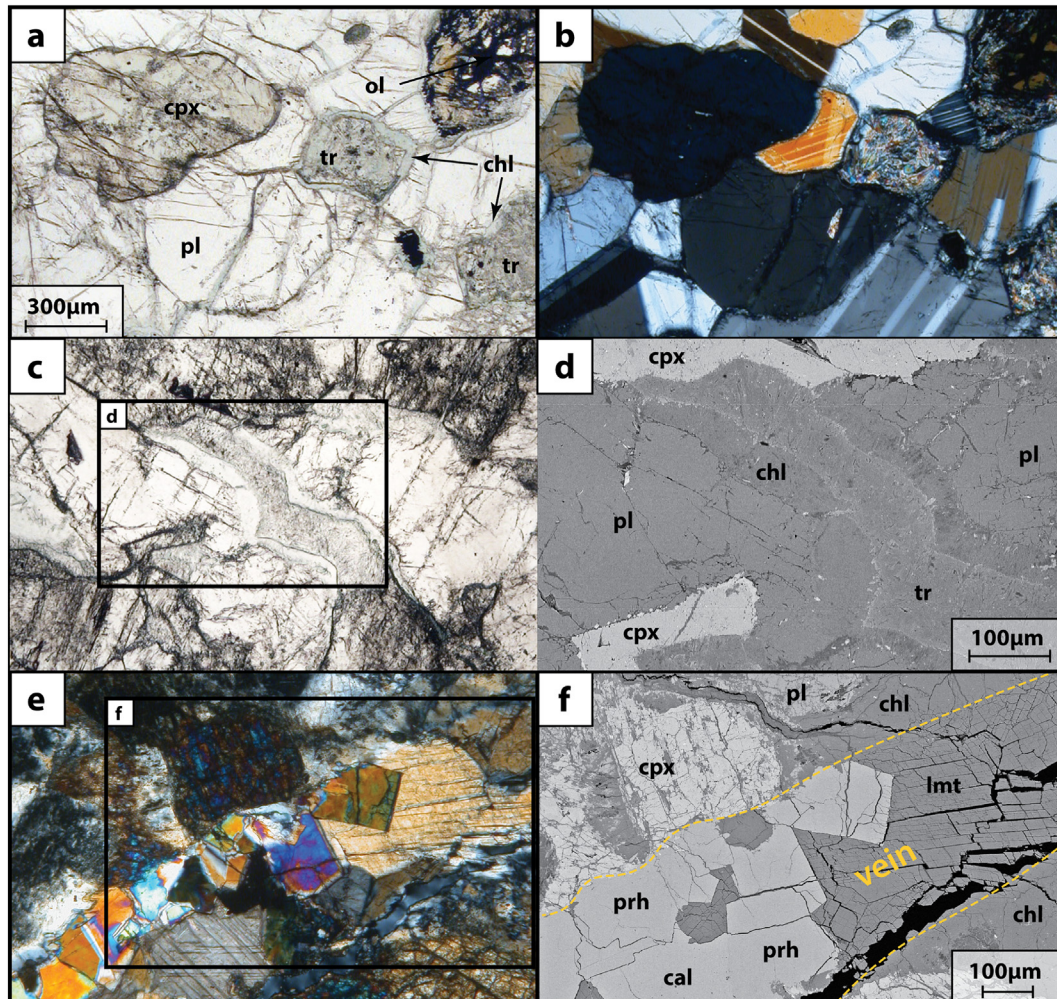


**Fig. 4.** Thin section photomicrographs of typical alteration pattern. (a) Background gabbro in plain-polarized light. Clinopyroxene is partially replaced by tremolite. Intact crystals show the formation of secondary oxides and partial overgrow of microcrystalline alteration phases. Plagioclase is well preserved, the formation of chlorite is focussed to grain boundaries. Olivine is heavily fractured and serpentinized, partially decomposed into iddingsite and opaque oxides, cores are mostly preserved. (b) Same area in cross-polarized light, revealing the mostly anhedral granular structure of tremolite and polysynthetic twinning of plagioclase. Note the microcrystalline chlorite at grain boundaries of plagioclase. (c & d) Plain polarized micrograph and BSE image of typical alteration within the footwall following the same systematics as for the background gabbros but forming veinlets by dissolving the magmatic phases. Pervasive disaggregation of clinopyroxene is more advanced. (e) Prehnite-laumontite vein through heavily altered gabbro of the hanging wall, in cross-polarized light. The magmatic assemblage is almost entirely replaced by pervasive fracturing-initiated alteration. The rock is intensely crosscut by a dense network of veins. Secondary phases, e.g., prehnite are well crystallized and intergrown with laumontite. (f) BSE image, details of a late vein, euhedral prehnite associated with laumontite and calcite. pl – plagioclase, cpx – clinopyroxene, ol – olivine, tr – tremolite, chl – chlorite, prh – prehnite, lmt – laumontite, cal – calcite.

actinolite needles. More altered clinopyroxenes show coronas of chlorite  $\pm$  tremolite when in contact with plagioclase. Plagioclases are more altered than clinopyroxenes, showing abundant fractures and partial replacement by fine-grained chlorite. Fresh olivine is absent. There are abundant veins in the hanging wall samples ranging from  $<10 \mu\text{m}$  to 1 mm width. Prehnite and prehnite-laumontite veins cross-cut earlier alteration phases and are being cross-cut by later laumontite-calcite veins (Fig. 4e, f).

#### 4.3. Clasts

The two clast samples (AH6, AH7) from the central part of the fault rock display variable degrees of alteration. Sample AH6 has a very similar alteration assemblage and intensity to the hanging wall samples but includes two ( $<1 \text{ mm}$ ) veinlets of brown hornblende, possibly formed during higher temperature ( $>500 \text{ }^\circ\text{C}$ ) hydrothermal alteration (Manning et al., 2000). Laumontite veins ( $<1 \text{ mm}$ ) cross-cut earlier alteration and are themselves cross-cut by later calcite veins. Late stage calcite also fills tiny open spaces between mineral grains, and appears to be the last alteration phase. In contrast, sample AH7 is almost completely altered with abundant calcite. Epidote partially replaces plagioclase and clinopyroxene. Clinopyroxene is mostly overgrown by

green hornblende, actinolite/tremolite and chlorite. As a whole, the sample is brecciated and cemented by calcite, with prominent calcite veins ( $\sim 1 \text{ mm}$ ) cross-cutting earlier alteration phases and veins.

#### 4.4. Chlorite-rich fault rock

Seven samples (AD5, AD6, AD7, DT-10, AH8, OM15-3C and OM15-3E) of the chlorite-fault rock have been analysed by thin section petrography. For all these samples the alteration intensity is close to 100%. The major constituents are chlorite (60–80%), epidote (5–15%), titanite ( $<5\%$ ), chalcocopyrite and pyrite ( $<5\%$ ) and pure copper ( $<5\%$ ). Moreover, most samples contain weathering products of sulphides such as iron-oxyhydroxides (5–10%), malachite (5%) as well as calcite (5–10%). In mineralized samples layered, fine-grained, concentric zonation (Fig. 5a, b) with variable contents of  $\text{SiO}_2$ , CuO and FeO (Fig. 5c) are common. Sample DT-10 is dominated by weathering products and consists mainly of iron-hydroxides (65%) and malachite (25%) with chlorite (10%) as a subordinate phase. Thin section petrography reveals the complete replacement of the original igneous minerals but a relict igneous texture is still visible (Fig. 5d). Radiating chlorite crystals ( $\sim 250 \mu\text{m}$ ) replace primary plagioclase and clinopyroxene and relict outlines of primary mineral grains remain visible in cross-polarized

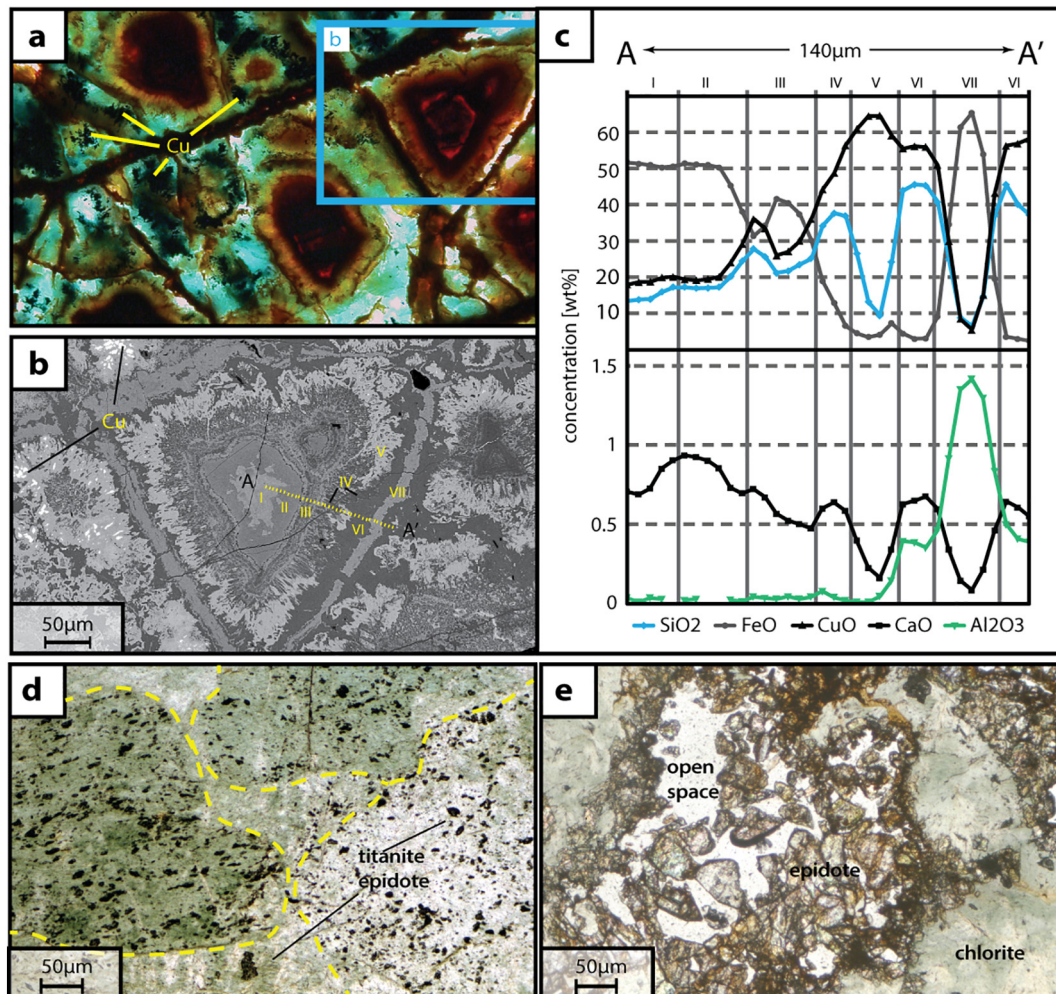


**Fig. 5.** Thin section micrographs of fault rock samples. (a) Chlorite-rich fault rock in plain polarized light showing concentric zoned alteration pattern of semi-opaque to opaque phases. Note the solid Cu nuggets. (b) BSE micrograph of concentric layered alteration revealing the complexity of zoning. (c) Major element composition along a profile from A to A'. Concentric zoned phases show variable contents of CuO, FeO and  $\text{SiO}_2$ . Zones are numbered according to (b). No primary phases are preserved. (d) Chlorite replacing initial magmatic minerals completely but outlines of former mineral grains still visible (yellow dotted lines). Chlorite is associated with fine-grained granular ( $<20 \mu\text{m}$ ) titanite and epidote. (e) Euhedral epidote crystals precipitated directly out of a hydrothermal fluid into open space. Associated chlorite is clean and does not co-exist with granular titanite and epidote suggesting precipitation from hydrothermal fluid rather than replacement of primary minerals as shown in (d).

light. This indicates that the chloritised fault rocks are strongly altered gabbros rather than sheared hydrothermal veins. Commonly, chlorite coexists with fine-grained, granular titanite (<20 µm) and epidote crystals (~50–100 µm) (Fig. 5e). Most samples show patches (1–5 mm) dominated by epidote, with euhedral crystals (100–250 µm) grown into open-space (Fig. 5e) that is partially filled by chlorite or secondary calcite. Typically, open-space filling chlorites are inclusion-free, and not associated with titanite, suggesting that it may be precipitated directly from a hydrothermal fluid instead of replacing primary minerals. Although chalcopyrite and pyrite grains are now only very small (5–20 µm) and rare in most samples, the numerous areas (>5 mm) with iron-hydroxides and malachite suggest they were previously abundant. Similar to the hanging wall, footwall and clast samples, calcite is the latest stage alteration mineral, mainly filling open spaces and thin veins that cross cut earlier alteration phases.

## 5. Mineral chemistry

### 5.1. Plagioclase

Plagioclase from the hanging wall and footwall samples is compositionally similar to plagioclase from the layered gabbro section elsewhere in the Wadi Tayin area (Pallister and Hopson, 1981). Most footwall plagioclase yield anorthite compositions ( $An_{75-81}$ ), slightly lower than the median composition of plagioclase in fresh layered gabbros ( $An_{82\pm 2\%}$ ) in Wadi Gideah (Fig. 6a; Table A3), but strongly albitised plagioclase are not present (< $An_{60}$ ). In contrast, plagioclase in the hanging wall rocks has very high anorthite contents (> $An_{90}$ ).

### 5.2. Amphibole

All measured amphiboles classify as Ca-amphiboles following the classification scheme of Leake et al. (1997) and compositions range from tremolite to actinolite, magnesiohornblende and tschermakite, with most analyses plotting in the tremolite-actinolite field (Fig. 6b; Table A4). All analysed amphiboles show compositions similar to amphiboles observed elsewhere in the ophiolite's gabbro section (Bosch et al., 2004) as well as in the plutonic section of modern oceanic crust (Alt et al., 2010). Amphiboles co-existing with chlorite in hanging and footwall samples have tremolite compositions with high Si and low  $Fe^{2+}$  abundances ( $Mg\# > 0.95$ ). In contrast, amphiboles replacing clinopyroxenes in hanging wall sample OM15-3A mainly plot in the magnesiohornblende field with a few tschermakite compositions. All measured amphiboles display low Cl concentrations of <0.05 wt.%.

### 5.3. Epidote

Epidote from the fault rock display a range of compositions with  $X_{Fe}$  ( $X_{Fe} = Fe/(Fe + Al)$ ) ranging between 0.2–0.34 (Table A5). This is somewhat higher than previously reported from epidote veins and epidote crystals in the alteration halos around hydrothermal veins in gabbros from the lower crustal section of Wadi Haymiliya in the central part of the ophiolite ( $X_{Fe} = 0–0.2$  for most analysis; Nehlig and Juteau, 1988). Similar  $X_{Fe}$  compositions of epidote with  $X_{Fe} = 0.17–0.36$  have been measured from the sheeted dikes and upper gabbros in ODP/IODP Hole 1256D (Alt et al., 2010).

### 5.4. Chlorite

Chlorite is the most abundant mineral in the fault rocks and also a major secondary phase in hanging wall and footwall samples. Chlorite replaces plagioclase and co-exists with tremolite along grain boundaries between plagioclase and pyroxene crystals. This is similar to how it is commonly observed in many ocean crustal rocks (e.g. Alt et al., 2010) as well as reported from experiments of gabbroic rocks with seawater

at temperatures between 300 and 475 °C (Beermann et al., 2017). Both in hanging wall and footwall samples chlorite replacing plagioclase and chlorite co-existing with tremolite display a narrow range in silica (5.3–6.1 Si pfu), in contrast to chlorite from elsewhere in the ophiolite (France et al., 2009; Nehlig and Juteau, 1988) and in modern oceanic crust (e.g. Alt et al., 2010) (Fig. 6c). Chlorites from the fault rocks yield a similar narrow range of silica but have considerably higher  $Fe/(Fe + Mg)$  ratios of 0.38 to 0.56 than hanging wall and footwall samples, with some samples being iron-rich,  $Fe/(Fe + Mg) > 0.55$  (Fig. 6c; Table A6). Furthermore, chlorite from the hanging and footwall gabbros have distinctive compositions too, with footwall chlorites  $Fe/(Fe + Mg)$  ratio at 0.23 to 0.3 being more iron-rich than hanging wall chlorites with  $Fe/(Fe + Mg)$  ratio from 0.18 to 0.22.

### 5.5. Prehnite and laumontite

Prehnite crystals from prehnite-laumontite veins have been analysed with the electron microprobe in the hanging wall sample OM15-3A (Table A7). Prehnite compositions are uniform with a calculated formula of  $Ca_{1.98-2}Na_{0-0.02}(Al_{0.96-0.98}Fe_{0.01-0.02}^{3+})Al_{0.94-0.97}Si_{3.03-3.06}O_{10}(OH)_2$ . Prehnite shows low iron concentrations with  $X_{Fe} = 100 * Fe/(Fe + Al^{IV})$  of 0.33–1.55. These results are comparable to the lowermost values reported by Nehlig and Juteau (1988) from late prehnite veins in the layered gabbro section of Wadi Haymiliya.

Laumontite in the prehnite-laumontite veins in hanging wall sample OM15-3A is homogeneous with low iron and sodium concentrations (Table A8). Calculated formula is  $Ca_{3.38-3.91}Na_{0-0.15}K_{0.01-0.39}(Al_{7.51-7.81}Fe_{0-0.13}Si_{16.19-16.44}) * 18H_2O$ .

## 6. Bulk rock major- and trace element compositions

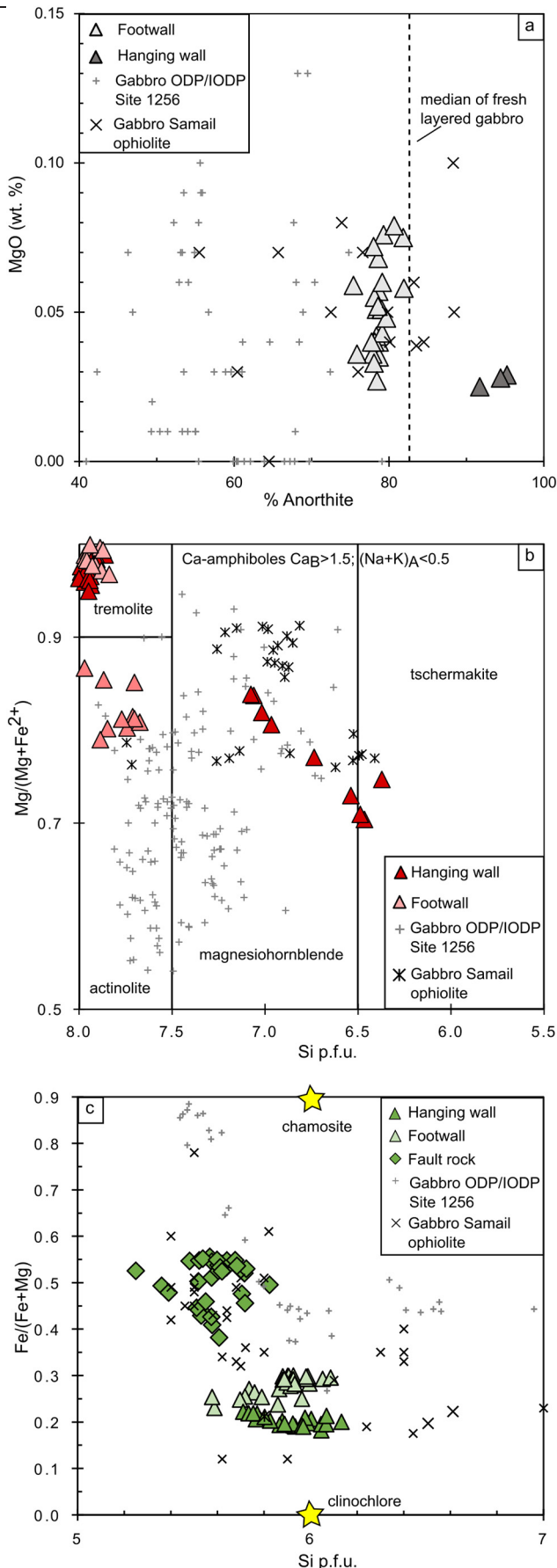
### 6.1. Fresh layered gabbro

Eight samples of fresh layered gabbro that crop out within 500 m of the fault zone have compositions typical of mafic cumulates from Wadi Tayin area (Peucker-Ehrenbrink et al., 2012), the Samail ophiolite in general (Browning, 1984; Pallister and Hopson, 1981; Pallister and Knight, 1981) and modern fast-spreading ocean ridges (Gillis et al., 2014). These rocks have magnesium numbers [ $Mg\# = 100 * (Mg^{2+}/(Mg^{2+} + Fe^{Total})_{atomic})$ ] that cluster in a narrow range of  $Mg\# = 88$  to 90 and incompatible minor and trace element concentrations (e.g.,  $K_2O$ ,  $TiO_2$ , Zr, Y, Nb) are low to very low, demonstrating the gabbros primitive compositions (Fig. 7; Table 1). Loss on ignition (L.O.I.) averages ~2 wt.%, indicating the presence of some minor alteration products. Chondrite-normalised (McDonough and Sun, 1995) rare earth element patterns show a depletion of the light rare earth element (LREE) and slightly decreasing abundance of the heavy rare earth elements (HREE). There is a strong positive Eu anomaly, reflecting the high modal abundance of plagioclase in the samples (Fig. 8).

### 6.2. Hanging and footwall samples

Relative to the unaltered layered gabbro, rocks from the hanging and the footwall have comparable major element compositions, with only subtle variations (Fig. 7). One hanging wall sample yields slightly lower values of CaO but still plots in the range of overall layered gabbro samples of the Wadi Tayin area (Peucker-Ehrenbrink et al., 2012). All three samples plot in the lower range of  $SiO_2$  concentration. The hanging and footwall samples have higher concentrations of volatiles with loss on ignition (L.O.I.) of 7.4 wt.% on average, indicating that they are more strongly altered than the fresh layered gabbro samples. Trace element concentrations are not significantly different compared to fresh layered gabbro concentrations (Fig. 7, Table 1), but tend to have slightly increased Sr concentrations and generally lower concentrations of Cu. Chondrite-normalised (McDonough and Sun, 1995) rare earth element pattern are identical to fresh layered gabbro (Fig. 8).





6.3. Clast samples

The two clast samples are slightly more variable in terms of major- and trace element composition when compared to hanging and footwall samples. The highly altered sample AH7 has clearly lower CaO and higher TiO<sub>2</sub> concentrations, similar to the chlorite fault rocks (Fig. 7; Table 1). Both clast samples show slightly higher concentrations for Na<sub>2</sub>O, possibly reflecting the presence of more albitic plagioclase as well as elevated volatile contents with L.O.I. 5 wt.% and 14.5 wt.%. Concentrations of V, Co, Zn and Ni are comparable to those of fresh olivine gabbro, whereas sample AH7 has a higher concentration for Cu. Rare earth element patterns are very similar to fresh layered gabbro although with a less pronounced Eu anomaly for the more altered sample AH7 (Fig. 8).

6.4. Chlorite-rich fault rocks

Major and trace element compositions of the chlorite-rich fault rock reflect the secondary mineral assemblage. All fault zone samples show high L.O.I. values of 8–17 wt.%, resulting from the high abundance of hydrous minerals such as chlorite and epidote and weathering products (e.g., malachite and iron oxyhydroxides). The chlorite-fault rock samples show different and more variable major elemental compositions compared to fresh layered gabbro (Fig. 7; Table 1). Total Fe<sub>2</sub>O<sub>3</sub> is up to six times higher than in fresh samples, whereas CaO, SiO<sub>2</sub> and Na<sub>2</sub>O concentrations are considerably lower. TiO<sub>2</sub> and MgO concentrations are slightly higher whereas Al<sub>2</sub>O<sub>3</sub> appears unchanged. In terms of minor and trace elements, the concentrations of Cu, Co, Zn and V are strongly increased compared to fresh gabbros for some of the samples. Cu concentrations are very high for some of the samples, reflecting the presence of chalcopyrite and its weathering products such as malachite. Strontium concentrations are generally lower than in fresh samples, in parallel with lower CaO values. Rare earth elements concentrations and patterns show some differences compared to fresh layered gabbro samples (Fig. 8): All samples display either no or negative Eu anomalies, compared to a positive anomaly in unaltered layered gabbro. This possibly reflects the disappearance of plagioclase. Furthermore, two samples yield significantly higher REE concentrations (up to 8× chondrite).

7. Strontium isotope compositions

Strontium isotope bulk compositions of six fault rock samples, two clast samples, three hanging and footwall samples were determined and are compared to eight fresh layered gabbro samples collected within 500 m of the fault zone outcrop. Additionally, epidote from an epidote vein in the footwall, laumontite from a laumontite-calcite vein in the hanging wall, and calcite from a calcite vein in the fault rock and from a calcite-laumontite vein in the hanging wall were

**Fig. 6.** (a) % Anorthite measured in feldspars from hanging wall and footwall samples vs MgO (wt.%) content. Compared to plagioclase composition of gabbros from modern ocean crust (Alt et al., 2010) and plagioclase of layered gabbros elsewhere in the Wadi Tayin massif (Pallister and Hopson, 1981). The dashed line represents the median value of % anorthite (An<sub>82±2%</sub>) measured in fresh layered gabbros of samples close to the fault zone outcrop (J. Koepke, unpublished data). High An-content of An<sub>91-95</sub> measured in fresh plagioclase suggest very primitive initial compositions. (b) Compositions of amphiboles measured in hanging wall and footwall samples compared to amphibole composition measured in layered gabbros elsewhere in the ophiolite (Bosch et al., 2004) and in the plutonic section of modern oceanic crust at ODP/IODP Site 1256 (Alt et al., 2010). Note the high amount of tremolite pointing towards a formation regime of high Mg concentration. (c) Compositions of chlorite replacing plagioclase and chlorite-tremolite patches in between plagioclase and pyroxene grains (Fig. 4b) measured in hanging wall and footwall samples in contrast to chlorite compositions of the fault rock. In comparison chlorite composition measured in upper and lower gabbros from Wadi Haymiliya in the central part of the ophiolite (Nehlig and Juteau, 1988), chlorite measured in isotropic high-level gabbros in Wadi Gideah (France et al., 2009) and chlorite compositions measured in gabbros of modern oceanic crust at ODP/IODP Site 1256 (Alt et al., 2010).

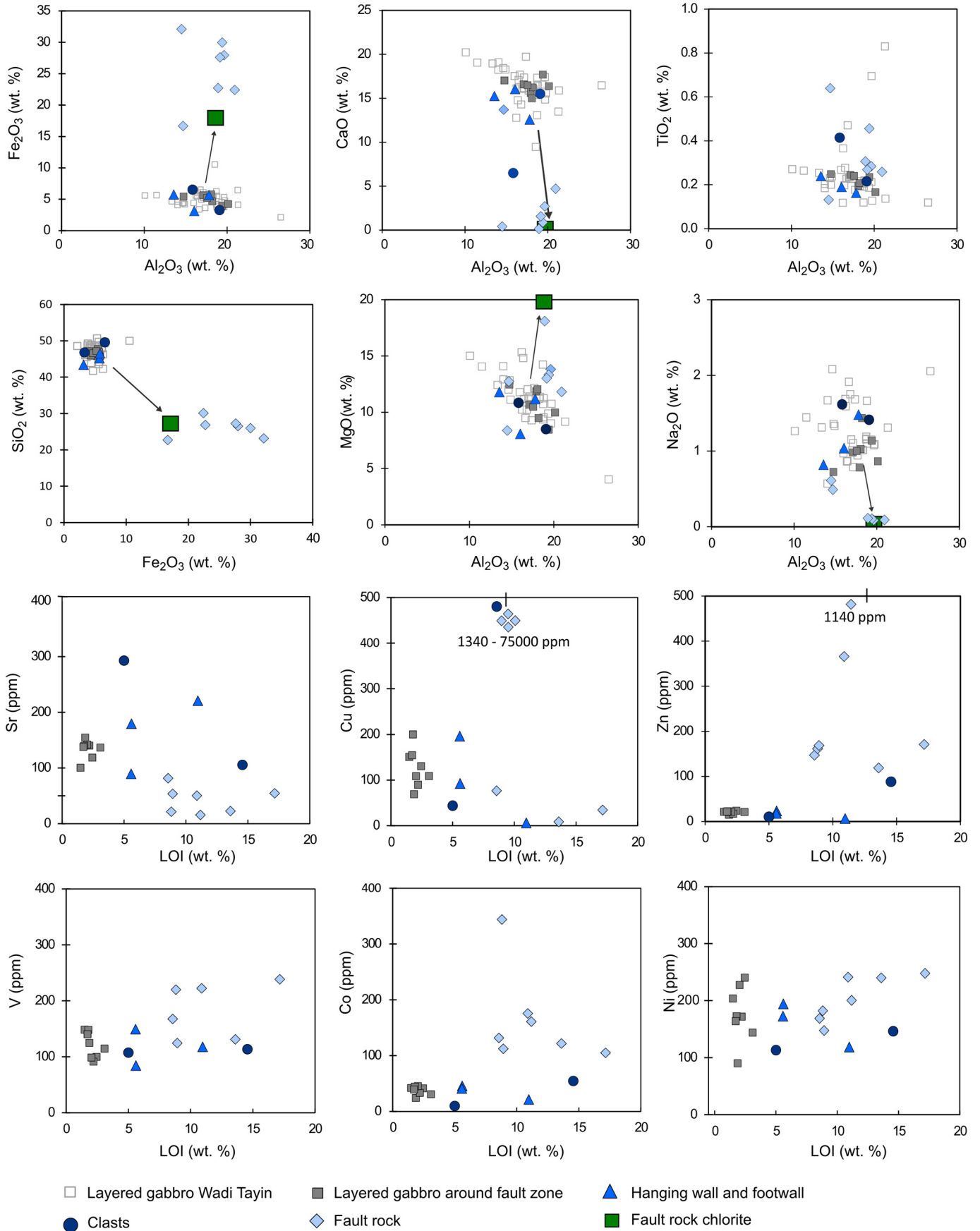


**Fig. 7.** Major- and trace element covariation diagrams for selected elements. Fault rock is shown in light blue diamonds, clast samples in dark blue circles, and hanging and footwall samples in royal blue triangles. Background layered gabbros are shown in grey squares and are from eight samples within a distance of 500 m to the fault zone outcrop. Open squares are olivine gabbro from elsewhere in Wadi Tayin (Peucker-Ehrenbrink et al., 2012). Green square represents the composition of chlorite measured in the fault rock and arrows indicate alteration vectors.

mechanically separated by hand picking (Fig. 9; Table 1). Fresh layered gabbros display a relatively narrow range of Sr concentrations (100–150 µg/g) and isotope compositions ( $^{87}\text{Sr}/^{86}\text{Sr} = 0.70299\text{--}0.70332$ ). These Sr-ratios are slightly elevated compared to fresh MORB ( $^{87}\text{Sr}/^{86}\text{Sr} = 0.70281$ ) from modern oceanic crust (White et al., 1987) and some show slightly more radiogenic values compared to fresh layered gabbro elsewhere in the Samail ophiolite ( $^{87}\text{Sr}/^{86}\text{Sr} \sim 0.70265\text{--}0.70320$ , McCulloch et al., 1980; Lanphere et al., 1981). The footwall sample plots with  $^{87}\text{Sr}/^{86}\text{Sr} = 0.70327$  close to fresh layered gabbro, indicating only very minor Sr isotopic exchange. In contrast, the hanging wall samples have more radiogenic values of  $^{87}\text{Sr}/^{86}\text{Sr} = 0.70390\text{--}0.70475$  compared to fresh layered gabbro ( $^{87}\text{Sr}/^{86}\text{Sr} = 0.70299\text{--}0.70332$ ), with sample OM15-3A also showing higher Sr concentration (221 µg/g) than fresh layered gabbro due to high abundance of hydrothermal laumontite and prehnite. The clast samples as well as the chlorite-rich fault rocks show a narrow range of strontium isotope composition ( $^{87}\text{Sr}/^{86}\text{Sr} = 0.70451\text{--}0.70450$ ), clearly shifted towards more radiogenic compositions, combined with low Sr concentrations compared to fresh layered gabbro (Sr = 50–100 µg/g). These Sr-isotope ratios are similar to the range of hydrothermal epidote and amphiboles, and highly altered gabbros from the Wadi Tayin area (e.g., Bosch et al., 2004; Coogan et al., 2006). Moreover, epidote from a monomineralic epidote vein of the footwall shows very similar Sr-isotope composition ( $^{87}\text{Sr}/^{86}\text{Sr} = 0.70428$ ). These epidote grains have euhedral crystal habits and appear to have precipitated directly out of a hydrothermal fluid and therefore should directly reflect the Sr-isotopic composition of the fluid.

The separated laumontite of sub-millimetre thick veinlets, cross-cutting all other alteration stages yields Sr-isotope ratios ( $^{87}\text{Sr}/^{86}\text{Sr} = 0.70737$ ) close to 95 Ma-seawater (Fig. 9). Hand-picked calcite of laumontite-calcite veinlets display the most radiogenic values of  $^{87}\text{Sr}/^{86}\text{Sr} = 0.70777\text{--}0.70823$  and plot in the range of Cretaceous to Miocene sediments (Weyhenmeyer, 2000) and close to the strontium isotope composition of modern groundwater ( $^{87}\text{Sr}/^{86}\text{Sr} = 0.7078$ ) from gabbro hosted wells in Wadi Tayin (pers. communication N. Bompard).

## 8. Discussion

### 8.1. Secondary mineralogy and hydrothermal fluid characteristics

Chlorite is a major constituent in both the fault rock as well as in hanging- and footwall gabbros and its composition can be used as a geothermometer to estimate alteration temperatures. Several studies report a systematic decrease of  $\text{Si}^{\text{IV}}$  coupled with an increase of  $\text{Al}^{\text{IV}}$  in chlorites with increasing temperature (Cathelineau, 1988; Cathelineau and Nieva, 1985; McDowell and Elders, 1980; Velde and Hillier, 1991). This correlation was used by Cathelineau (1988) to develop an empirical geothermometer of general applicability in diagenetic, hydrothermal and metamorphic settings based on the incorporation of  $\text{Al}^{\text{IV}}$ . Several studies show that the  $\text{Al}^{\text{IV}}$ -temperature correlation is likely to be influenced by the  $\text{Fe}/(\text{Fe} + \text{Mg})$  ratio of the chlorite (Jowett, 1991; Kranidiotis and MacLean, 1987) and the empirical geothermometer of Cathelineau (1988) was extended by a correction factor (Jowett, 1991). Using this adapted thermometer of Jowett (1991) we calculate temperatures of chlorite formation in the fault rock as well as chlorite in hanging wall and footwall (supplementary Fig. A9\_3; Table A6). The majority of fault rock chlorites show formation temperatures between 300 and 350 °C (median temperature 330 °C), whereas hanging wall and footwall chlorite show a slightly larger spread of temperatures but most plot in the range of ~250–300 °C with a median temperature of 275 °C for footwall and 268 °C hanging wall chlorite (Supplementary Fig. A9\_3). Statistical analysis on the temperature range of all three lithology's show that the temperature difference between fault rock and both wall rocks are significant (see box plot in Fig. A9\_3). However, petrographic observations indicate that chlorites of the fault and

chlorites within the walls have formed at different conditions (e.g. different fluid/rock ratio, pH and time). Therefore, an additionally influence of the host rock composition on the chlorite formation temperature as stated by Xie et al. (1997) cannot be entirely ruled out (e.g.  $\text{Fe}_2\text{O}_3$  content is very different between hanging- and footwall: ~5 wt% and fault rock: ~25 wt%; see Table 1). The difference in chlorite formation temperatures between the fault rock (~300–350 °C) and the hanging- and footwall (~250–300 °C) suggest an open system of multi-stage alteration and a fluid evolution towards a highly charged composition. The formation of chlorite in the hanging- and footwall during initial fluid migration along the fault at slightly lower temperatures (~250–300 °C), subsequent evolution and channeling of the hydrothermal fluids, accompanied by a temperature rise to 300–350 °C, re-equilibrating the chlorite along the fault but not the chlorite in the wall rocks, is a likely scenario.

The fault rock and clast samples have similar Sr-isotope compositions (Fig. 9) as the epidote vein in the footwall as well as epidote veins observed elsewhere in the ophiolite (e.g., Bosch et al., 2004; Coogan et al., 2006). The epidotes have relatively high Sr concentrations (400 to 750 µg/g) and are robust against low-temperature fluid-rock Sr exchange and hence analyses of epidote precipitated in veins are commonly used to estimate the Sr-isotopic compositions of the hydrothermal fluids (e.g., Bickle and Teagle, 1992; Harris et al., 2015; Teagle et al., 2003). Epidotes, equigranular epidote-quartz-titanite rocks, are present in the sheeted dike complexes of many ophiolites, and thought to record zones of concentrated “black smoker-type” hydrothermal upwelling fluid flow (e.g., Richardson et al., 1987; Schiffman et al., 1987) and have similar Sr-isotopic compositions to epidote veins. The Oman epidote  $^{87}\text{Sr}/^{86}\text{Sr}$  ratios are clearly elevated relative to fresh layered gabbro indicating the extensive exchange of the rock with a seawater-derived hydrothermal fluid. We propose that this fluid had a  $^{87}\text{Sr}/^{86}\text{Sr}$  in the range of 0.7043–0.7048, and that the passage of a black smoker-like fluid with this Sr-isotopic composition resulted in the alteration of the fault rocks, clasts and surrounding wall rocks.

The degree of alteration, the strontium isotopic composition of the fault rock and particularly the observed secondary mineral assemblage with abundant Cu-sulphides suggest a formation of the fault rock during fluid-rock interactions with up-welling, discharging hydrothermal fluids at chlorite formation temperatures of about 300–350 °C. Hints towards enhanced fluid recharge activity are absent in this fault. Minor but pervasive replacement of clinopyroxene by Mg-hornblende in the altered clast and hanging wall samples indicates an earlier phase of higher temperature hydrothermal alteration which is now mostly overprinted by the described, lower-temperature alterations.

### 8.2. Mass changes during hydrothermal fluid-rock interaction

#### 8.2.1. Calculating mass changes

Comparison of altered bulk rock composition with relatively fresh rocks allow us to estimate the effects of hydrothermal alteration more quantitatively. These calculations indicate which elements are either immobile, mobilized or precipitated, and ultimately lost or gained during fluid-rock interactions. To calculate net mass changes, it is essential that altered rocks are compared with appropriate precursor compositions. Widely available analyses for fresh Oman gabbros makes this simpler than in more complex or metamorphosed terranes. A widely applied method to monitor changes during hydrothermal alteration uses the behaviour of immobile elements that are passively concentrated or diluted by whole rock mass loss or mass gain, respectively (Grant, 1986; Gresens, 1967; MacLean, 1990; MacLean and Barrett, 1993). Therefore, concentration ratios of these immobile elements in the rock before and after alteration can be used to calculate changes of other, mobile elements. Grant (1986) re-defined the original equation of Gresens (1967), relating the concentration of an element  $i$  in the altered rock to the concentration of the same element in the precursor

**Table 1**  
Mineral paragenesis, whole rock major- and trace element data and Sr-isotope data of all samples.

Typ		Fresh background gabbro <sup>a</sup>	Hanging wall	Hanging wall	Footwall	Clast	Clast	Fault rock	Fault rock	Fault rock	Fault rock	Fault rock	Fault rock	Fault rock	
Sample ID		Md ± MAD (n=8) <sup>b</sup>	AH9	OM15-3A <sup>d</sup>	OM15-3F <sup>d</sup>	AH6	AH7	AD5	AD6	AD7	DT-10	OM15-3C <sup>d</sup>	OM15_3E <sup>d</sup>	AH8	
<b>Mineral assemblage</b>	<b>Primary minerals</b>	Plagioclase, clinopyroxene, olivine ± oxides	Clinopyroxene and plagioclase partially preserved	Clinopyroxene and plagioclase partially preserved	Clinopyroxene and plagioclase partially well preserved	Clinopyroxene and plagioclase partially preserved	Clinopyroxene and plagioclase only rarely preserved	No primary minerals preserved	No primary minerals preserved	No primary minerals preserved	No primary minerals preserved	No primary minerals preserved	No primary minerals preserved	Some clinopyroxene relics preserved	
	<b>Secondary minerals</b>	± Chlorite, ± Mg-hornblende, chlorite, ± tremolite	Albite, Mg-hornblende, actinolite, chlorite, prehnite, laumontite	Prehnite, chlorite, laumontite, Mg-hornblende, pumpellyite	Chlorite, tremolite, Mg-hornblende, oxides	Albite, Mg-hornblende, actinolite, laumontite carbonate, ± epidote, ± titanite	Chlorite, albite, Mg-hornblende, actinolite, epidote	Chlorite, epidote, titanite	Chlorite, epidote, titanite	Chlorite, epidote, titanite, chalcopyrite	Chlorite	Chlorite	Chlorite	Chlorite, epidote	Chlorite, epidote, titanite
	<b>Weathering minerals</b>	-	Minor amount of Fe-hydroxides, calcite	Calcite, Fe-hydroxides	-	-	Calcite	Fe-hydroxides, calcite	Fe-hydroxides, malachite, calcite	Fe-hydroxides, malachite, calcite	Fe-hydroxides, malachite, calcite	Fe-hydroxides, malachite, calcite	Fe-hydroxides, malachite, pure Cu, calcite	Calcite, malachite	Fe-hydroxides, malachite, calcite
	<b>Vein</b>	Hornblende Tremolite Chlorite Prehnite Zeolite Calcite		x x x x x	x x x	x x x	x x x	x x x	x x x	x x x	x x x	x x x	x x x	x x x	x x x
<b>SiO<sub>2</sub></b>	wt. % XRF	46.72 ± 0.6	45.2	43.4	46.5	46.8	49.6	26.5	26	30.1	23.2	27.2	22.7	26.9	
<b>Al<sub>2</sub>O<sub>3</sub></b>	wt. % XRF	17.99 ± 0.7	17.8	16	13.6	19.1	15.8	19.6	19.4	20.9	14.5	19.2	14.7	18.9	
<b>Fe<sub>2</sub>O<sub>3</sub></b>	wt. % XRF	5.28 ± 0.4	5.7	3.2	5.8	3.3	6.6	28	30	22.4	32.1	27.6	16.7	22.7	
<b>MnO</b>	wt. % XRF	0.09 ± 0.01	0.1	0.1	0.1	0.1	0.1	0.3	0.3	0.2	0.3	0.3	0.2	0.2	
<b>MgO</b>	wt. % XRF	10.58 ± 1.2	11.2	8.1	11.8	8.5	10.8	13.8	13.3	11.8	8.4	13	12.7	18.1	
<b>CaO</b>	wt. % XRF	16.44 ± 0.4	12.6	16.1	15.3	15.5	6.5	2.7	0.9	4.7	0.4	1.6	13.7	0.2	
<b>Na<sub>2</sub>O</b>	wt. % XRF	0.99 ± 0.1	1.5	1	0.8	1.4	1.6	0.1	0.1	0.1	0.6	<0.2	0.5	0.1	
<b>K<sub>2</sub>O</b>	wt. % XRF	<0.02	<0.01	0.04	0.01	<0.01	<0.01	<0.01	<0.01	<0.01	0.02	<0.02	<0.02	<0.01	
<b>TiO<sub>2</sub></b>	wt. % XRF	0.22 ± 0.02	0.2	0.2	0.2	0.2	0.4	0.3	0.5	0.3	0.1	0.3	0.6	0.3	
<b>P<sub>2</sub>O<sub>5</sub></b>	wt. % XRF	<0.08	0.01	<0.08	<0.08	0.01	0.02	0.02	0.03	0.01	0.1	0.01	0.1	0.01	
<b>SO<sub>3</sub></b>	wt. % XRF	-	<0.01	<0.01	<0.01	<0.01	0.02	0.01	<0.01	<0.01	0.01	0.01	0.02	<0.01	
<b>L.O.I.<sup>c</sup></b>	wt. % XRF	1.95 ± 0.2	5.6	11	5.6	5	14.6	8.6	8.8	8.9	11.2	10.9	17.2	13.6	
<b>Total</b>	wt. % XRF	100	99.8	99.1	99.7	99.8	99.6	99.8	99.2	99.5	90.8	100	99.1	99.8	
<b>Mg#</b>		88-90	88.6	91	89	91.1	86.8	66.2	63.8	67.6	50.8	65.1	75.1	75.9	
<b>Li</b>	µg/g ICP-MS/LA-ICP MS	0.82 ± 0.2	0.7	0.4	0.3	0.2	1.1	0.8	0.6	1	0.8	2.2	1.4	0.9	
<b>Sc</b>	µg/g ICP-MS/LA-ICP MS	41.77 ± 6.4	33.3	33.5	46.7	39.7	51.7	53.7	51.1	44.6	27.7	50.1	51.1	44.8	
<b>V</b>	µg/g ICP-MS/LA-ICP MS	119.74 ± 20.9	84.3	117.6	149.2	107.3	113.5	167.6	219.7	124.5	1547	222.3	238.5	131.2	
<b>Cr</b>	µg/g XRF/LA-ICP-MS	685.34 ± 109.3	548.2	366.6	651.2	437.7	798.1	581.4	642.5	531.1	409	743.8	806.4	1140.7	
<b>Co</b>	µg/g XRF/LA-ICP-MS	40.32 ± 4.6	45.6	21.3	41.1	9.9	54.5	131.8	344	112.3	161	175.3	105.1	121.5	
<b>Ni</b>	µg/g XRF/LA-ICP-MS	172.15 ± 30.1	194.4	118.6	172.7	113.2	146.2	168.9	182.2	147.4	200.3	241	247.8	240	
<b>Cu</b>	µg/g ICP-MS/LA-ICP MS	119.71 ± 30.4	92.8	6.4	196.4	44	1339	76.7	4557	3406	75790	6514.2	34.6	8.8	
<b>Zn</b>	µg/g ICP-MS/LA-ICP MS	21.68 ± 1	23.3	6.8	18.2	10.5	88.1	147.3	161.5	168.6	1141	366.1	170.8	119	
<b>Rb</b>	µg/g ICP-MS/LA-ICP MS	0.08 ± 0.01	0.1	0.1	0.1	0.1	0.1	0.01	0.01	0.02	0.02	0.1	0.1	0.01	
<b>Sr</b>	µg/g ICP-MS/LA-ICP MS	139.16 ± 2.8	179.5	221.1	89.7	292.9	105.7	81.7	21.4	53.7	15.7	50.4	54.6	22.8	

<b>Y</b>	µg/g	XRF/LA ICP-MS	4.32 ± 0.5	6.6	4.2	5.8	7.8	10.1	7.5	13.2	5.9	3	6.4	12	8.1
<b>Zr</b>	µg/g	XRF/LA ICP-MS	3.21 ± 0.3	7.6	2.9	3.7	8.3	13.6	5.1	16.5	6	4.8	4.8	-	11.1
<b>Cs</b>	µg/g	ICP-MS/LA- ICP MS	<0.01	0.002	0.004	0.003	0.001	0.001	0.001	<0.0003	0.002	0.001	0.007	0.003	<0.0003
<b>Ba</b>	µg/g	ICP-MS/LA- ICP MS	2.21 ± 0.2	5.5	3.1	7.4	9.3	3.6	<0.45	<0.45	3.7	0.6	14	9	<0.45
<b>La</b>	µg/g	ICP-MS/LA- ICP MS	0.21 ± 0.02	0.1	-	0.2	0.1	0.2	0.9	0.2	0.3	0.1	0.2	0.6	0.1
<b>Ce</b>	µg/g	ICP-MS/LA- ICP MS	0.63 ± 0.1	0.5	-	-	0.5	0.8	2.8	1	0.8	0.5	0.7	2.7	0.5
<b>Pr</b>	µg/g	ICP-MS/LA- ICP MS	0.14 ± 0.02	0.1	0.1	0.2	0.1	0.2	0.5	0.2	0.2	0.1	0.1	0.5	0.1
<b>Nd</b>	µg/g	ICP-MS/LA- ICP MS	0.93 ± 0.1	0.7	0.8	1	0.8	1.3	2.9	1.4	1.1	0.6	0.9	3.1	1
<b>Sm</b>	µg/g	ICP-MS/LA- ICP MS	0.44 ± 0.1	0.3	0.4	0.5	0.4	0.6	0.9	0.8	0.5	0.3	0.5	1.3	0.5
<b>Eu</b>	µg/g	ICP-MS/LA- ICP MS	0.29 ± 0.01	0.2	0.2	0.3	0.2	0.4	0.4	0.2	0.2	0.1	0.2	0.5	0.2
<b>Gd</b>	µg/g	ICP-MS/LA- ICP MS	0.68 ± 0.1	0.5	0.6	0.8	0.7	1	1.2	1.4	0.8	0.5	0.8	1.7	0.8
<b>Tb</b>	µg/g	ICP-MS/LA- ICP MS	0.12 ± 0.02	0.1	-	-	0.1	0.2	0.2	0.3	0.2	0.1	0.2	0.3	0.2
<b>Dy</b>	µg/g	ICP-MS/LA- ICP MS	0.83 ± 0.1	0.7	0.7	1.1	0.8	1.3	1.3	1.8	1	0.7	1.2	2.1	1
<b>Ho</b>	µg/g	ICP-MS/LA- ICP MS	0.18 ± 0.02	0.1	0.2	0.2	0.2	0.3	0.3	0.4	0.2	0.2	0.3	0.4	0.2
<b>Er</b>	µg/g	ICP-MS/LA- ICP MS	0.47 ± 0.1	0.4	0.4	0.6	0.5	0.8	0.8	1.1	0.6	0.5	0.7	1.3	0.6
<b>Tm</b>	µg/g	ICP-MS/LA- ICP MS	0.07 ± 0.01	0.1	0.1	0.1	0.1	0.1	0.1	0.2	0.1	0.1	0.1	0.2	0.1
<b>Yb</b>	µg/g	ICP-MS/LA- ICP MS	0.41 ± 0.1	0.3	0.4	0.5	0.4	0.7	0.7	0.9	0.5	0.5	0.6	1.2	0.5
<b>Lu</b>	µg/g	ICP-MS/LA- ICP MS	0.06 ± 0.01	0.1	0.1	0.1	0.1	0.1	0.1	0.1	0.1	0.1	0.1	0.2	0.1
<b>Hf</b>	µg/g	ICP-MS/LA- ICP MS	0.15 ± 0.02	0.3	0.1	0.2	0.3	0.3	0.2	0.4	0.2	0.2	0.2	-	0.4
<b>Pb</b>	µg/g	ICP-MS/LA- ICP MS	10.83 ± 10.6	<0.08	0.03	0.1	<0.08	<0.08	<0.08	0.5	0.1	3.3	0.7	0.2	<0.08
<b>Th</b>	µg/g	ICP-MS/LA- ICP MS	<0.005	0.01	0.003	0.004	0.01	0.01	0.01	0.02	0.01	0.02	0.01	0.08	0.01
<b>U</b>	µg/g	ICP-MS/LA- ICP MS	<0.005	0.02	0.01	0.01	0.01	0.06	0.02	0.6	0.05	10.2	0.2	0.04	0.01
<b><sup>87</sup>Sr/<sup>86</sup>Sr measured</b>				0.703903	0.704756	0.703274	0.704510	0.704969	0.704553	-	0.704742	0.705480	0.704745	0.704802	-
<b><sup>87</sup>Sr/<sup>86</sup>Sr 95 Ma</b>				0.703900	0.704754	0.703269	0.704508	0.704965	0.704553	-	0.704741	0.705444	0.704741	0.704792	-
<b>±2 SE (error)</b>				14	13	14	16	16	16	-	16	14	12	11	-
Picked minerals		Foot wall		Hanging wall		Hanging wall		Fault rock							
		Epidote (vein)		Laumontite (vein)		Calcite (vein)		Calcite (vein)							
<b><sup>87</sup>Sr/<sup>86</sup>Sr measured</b>		0.704280		0.707378		0.708242		0.707778							
<b><sup>87</sup>Sr/<sup>86</sup>Sr 95 Ma</b>		0.704279		0.707366		0.708233		0.707767							
<b>±2 SE</b>		14		17		14		14							

<sup>a</sup> Major elements measured with ICP-OES, trace elements measured with liq.-ICP-MS and LA-ICP-MS, for details see Table A1 for detail.

<sup>b</sup> Median ± median absolute deviation, see Table A1 for detail.

<sup>c</sup> L.O.I. determined by loss-on-ignition experiment at 1000 °C.

<sup>d</sup> Trace elements measured with LA-ICP-MS on pressed powder tablets.

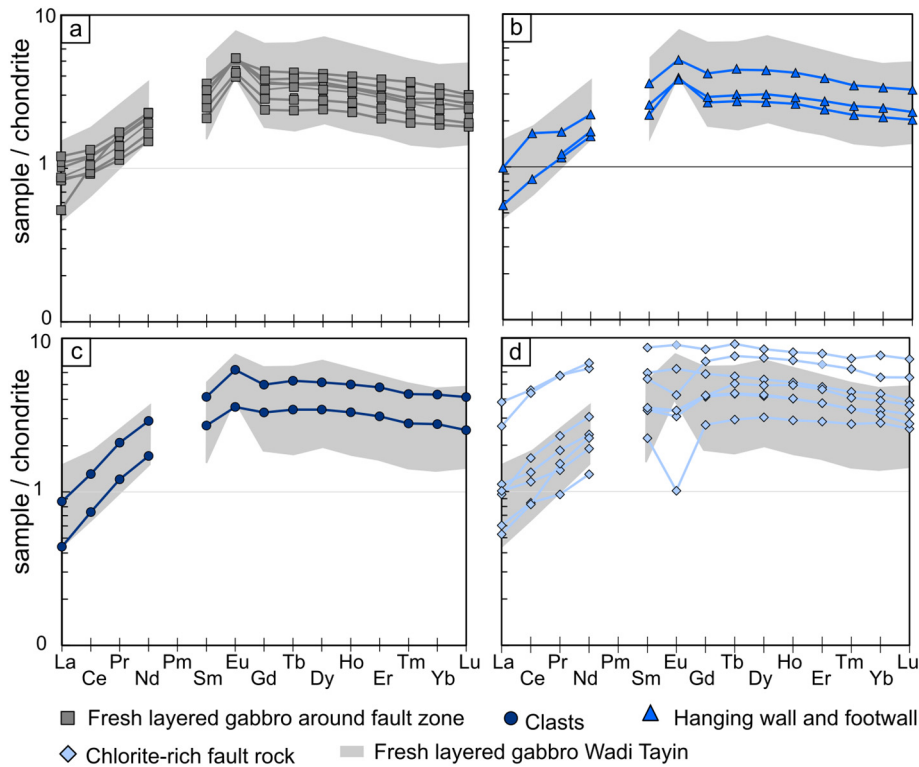


**Fig. 8.** Chondrite-normalised REE for (a) background layered gabbros, (b) hanging wall and footwall, (c) clasts, and (d) chlorite-rich fault rock. Chondrite values from McDonough and Sun (1995). The shaded grey area represents chondrite-normalized REE of olivine gabbro observed elsewhere in the Wadi Tayin (Peucker-Ehrenbrink et al., 2012).

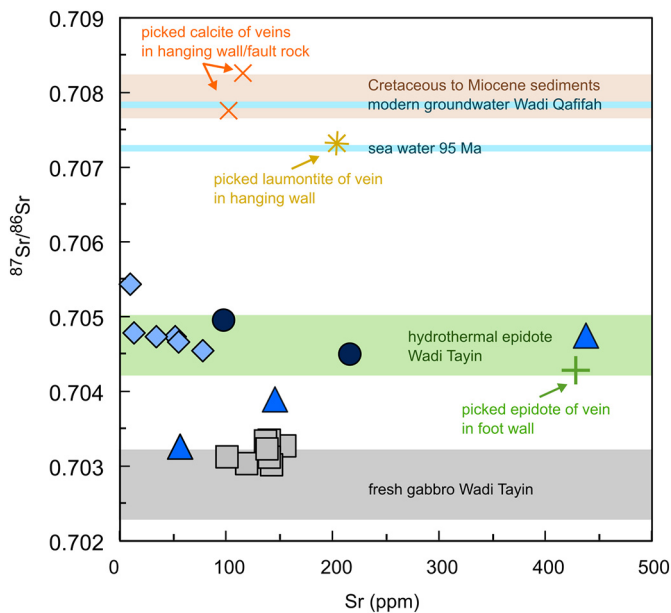


**Fig. 9.**  $^{87}\text{Sr}/^{86}\text{Sr}$  vs Sr content ( $\mu\text{g}/\text{g}$ ) of fresh layered gabbro within 500 m distance of the fault zone outcrop (grey squares), hanging and footwall samples (blue triangles), clast samples (dark blue dots), chlorite-rich fault rock (light blue diamonds), picked epidote from an epidote vein in the footwall (green cross), picked laumontite of a laumontite-calcite vein in the hanging wall (yellow star) and two picked calcite samples of a calcite vein within the fault rock and a calcite-laumontite vein in the hanging wall (orange crosses). Values of fresh layered gabbro of Wadi Tayin after Lanphere et al. (1981); McCulloch et al. (1981), Cretaceous seawater from McArthur et al. (2001), modern groundwater sampled in gabbro hosted wells of Wadi Qafifah (personal communication N. Bompard) and values of Cretaceous to Miocene sediments from Weyhenmeyer (2000).

rock through a mass change term ( $\frac{M^0}{M^A}$ ). The change of concentration of element  $i$  during alteration is the difference between the concentration of element  $i$  before ( $c_i^0$ ) and after ( $c_i^A$ ) alteration. The equation is formulated as:

$$c_i^A = \frac{M^0}{M^A} (c_i^0 + \Delta c_i) \quad (1)$$

where  $c_i^A$  = concentration of component  $i$  in the altered rock,  $c_i^0$  = concentration of element  $i$  in the precursor rock,  $M^0$  = mass of the precursor rock,  $M^A$  = mass of the altered rock and  $\Delta c_i$  = change in concentration of element  $i$ . This equation describes a straight line with a slope defined by the mass change term ( $\frac{M^0}{M^A}$ ) and the y-axis intercept ( $\frac{M^0}{M^A} * \Delta c_i$ ).

To calculate elemental gains and losses for each altered sample, precursor compositions need to be defined. In the case of the chlorite-rich fault rock within the layered gabbros presented here, a single precursor system is assumed, as the layered gabbros are chemically reasonably homogenous (Figs. 7 & 8). For this study, the median concentrations of eight samples of the fresh layered gabbro within 500 m of the fault zone outcrop was taken as a precursor composition (Table A2). To select which elements can be considered as immobile and are, therefore, appropriate for calculating the mass change term, each of the seven samples from the chlorite-fault zone was examined individually, by comparing the concentration of element  $i$  in the altered rock ( $c_i^A$ ) to the median value of the precursor rock ( $c_i^0$ ). For all the fault-rock samples the  $c_i^A/c_i^0$  for HREE cluster together (Fig. 10). Hence, we have selected the HREE (Dy and heavier) to calculate the mass change term ( $\frac{M^0}{M^A}$ ).

### 8.2.2. Chemical changes during hydrothermal alteration

Results of mass change calculations are summarized in Table 2 and median mass changes are plotted in Fig. 10. Chlorite-rich fault rock



Table 2 (continued)

	Chlorite fault rock														Med (n = 7)	MAD (n = 7)
	AD5		AD6		AD7		DT-10		OM15-3C		OM15_3E		AH8			
	wt. %,	%	wt. %,	%	wt. %,	%	wt. %,	%	wt. %,	%	wt. %,	%	wt. %,	%		
	µg/g		µg/g		µg/g		µg/g		µg/g		µg/g		µg/g			
Sr	−88.9	−63.9	−129.6	−93.1	−97	−69.7	−123.3	−88.6	−105.9	−76.1	−118.7	−85.3	−120.7	−86.8	−85.3	8.4
Y	0.3	7.1	1.6	36.3	0.3	6.2	−1.3	−29.8	−0.1	−1.5	0.2	4	2.2	51.3	6.2	17.4
Zr	−0.1	−2.3	4.2	129.2	1.5	45.5	1.6	51	−0.04	−1.2	—	—	5.8	179	48.3	52.2
Cs <sup>a</sup>	−0.004	−87.5	—	—	−0.003	−68	−0.004	−79.4	−0.0001	−1.1	−0.004	−74.3	—	—	−74.3	49.3
Ba	—	—	—	—	0.7	31.3	−1.6	−71.6	7.0	317.2	1.2	52.7	—	—	42	134
La	0.3	168.6	−0.1	−50.9	0.0004	0.2	−0.1	−30.3	−0.05	−23.6	0.03	13.8	−0.1	−51.3	−23.6	45
Ce	1.1	173.2	−0.2	−28.5	0.01	1.4	−0.1	−17	−0.2	−25.8	0.4	58.5	−0.2	−35.3	−17	46.1
Pr	0.2	136.8	−0.04	−30.7	−0.003	−2.1	−0.05	−34.7	−0.1	−38.8	0.1	42.8	−0.02	−17.4	−17.4	40.2
Nd	0.8	90.2	−0.3	−33.1	−0.1	−9.8	−0.3	−35.8	−0.4	−38.5	0.2	25.6	−0.1	−11.7	−11.7	30.5
Sm	0.1	22.7	−0.1	−18.8	−0.05	−11.2	−0.1	−24.3	−0.1	−24.7	0.04	8.8	−0.02	−4.6	−11.2	13.5
Eu	−0.1	−24.3	−0.2	−63	−0.1	−48.5	−0.2	−80	−0.2	−60.2	−0.1	−34.3	−0.1	−46.7	−48.5	14
Gd	0.03	4.9	−0.1	−8.2	−0.03	−5.1	−0.1	−19.8	−0.1	−19.2	−0.1	−7.8	−0.0003	−0.05	−7.8	6.7
Tb	0.00002	0.01	−0.002	−1.8	−0.003	−2.7	−0.02	−14.2	−0.005	−4	−0.002	−1.4	0.002	1.5	−1.8	3
Dy	−0.02	−2.1	−0.02	−1.9	−0.02	−2.7	−0.1	−8.9	−0.03	−4.1	−0.1	−6.4	0.02	2.1	−2.7	2.5
Ho	−0.004	−2.1	−0.002	−1.2	−0.004	−2.5	−0.02	−8.7	0.002	1.1	−0.01	−6.3	0.002	0.9	−2.1	2.6
Er	−0.0001	−0.02	0.01	1.5	−0.002	−0.4	−0.01	−2.2	0.02	3.5	−0.0001	−0.03	0.01	3	−0.02	1.5
Tm	0.002	2.5	0.003	4.7	0.001	0.9	0.003	4.1	0.0004	0.6	0.002	2.5	0.003	3.9	2.5	1.2
Yb	0.02	4.6	−0.01	−3	0.02	4	0.04	10.9	0.01	1.4	0.1	13	−0.001	−0.2	4	4.3
Lu	−0.002	−2.8	−0.0001	−0.2	0.0004	0.6	0.003	4.8	−0.001	−2.3	0.01	10.3	−0.01	−9.7	−0.2	4.4
Hf	−0.02	−10.9	0.03	18.4	0.03	17.1	0.1	39.7	−0.01	−8.4	0.8	513.8	0.1	96.9	18.4	93.2
Pb	—	—	−10.6	−98.1	−10.7	−99.1	−7.5	−69.6	−10.4	−96	−10.7	−99.2	—	—	−98.1	114.5
U	0.004	72.8	0.1	1058.9	0.03	533	10.3	181558.3	0.1	1819.6	0.03	167.5	0.004	70.1	533	26303.8
Mass change term	1.6		2.3		1.3		1		1.5		2.7		1.2		1.7	
Total mass change (%)																−67.0

<sup>a</sup>Cs is median value of Cs from layered gabbros in Wadi Tayin published in Peucker-Ehrenbrink et al., 2012.

samples show on average a significant mass loss of 67% and clast samples a loss of 34%. In contrast, there is no significant mass change (−1%) for hanging and footwall samples. Major element changes are variable, both within and between the three rock types, mainly reflecting differences in the secondary mineral assemblages formed and the extent of fluid-rock exchange.

SiO<sub>2</sub> is slightly to highly reduced in all samples with increasing alteration (Fig. 10). Chlorite fault rock samples have lost >60% of their silica compared to fresh layered gabbro. This is a substantial part of the total mass loss calculated for chlorite-rich rocks. There is no altered gabbro sample showing any silica enrichment. This agrees well with the absence of secondary quartz and suggests that silica has been transported away from these rocks by the passage of hydrothermal fluids. The general silica loss due to hydrothermal alteration of oceanic crust has been described previously (e.g. Coggon et al., 2016). The behaviour of silica in hydrothermal fluids is relatively well understood (Von Damm et al., 1991), and the silica-loss (63%) from the chlorite-rich fault zones can be used to calculate how much fluid has flowed through this fault zone. The solubility of SiO<sub>2</sub> in hydrothermal fluids principally depends on temperature, pressure and salinity. Using the quartz solubility in seawater of 15.7 and 31.2 mmol/kg, at 300 and 400 °C, respectively (Von Damm et al., 1991), results in fluid/rock ratios between 450:1 to 900:1. This estimation is possibly an upper limit as some mid-ocean ridge hydrothermal fluids have salinities greater than seawater, and quartz solubility increases with increasing salinity (Xie and Walther, 1993), but it assumes that the mobilisation of silica is 100% efficient. Regardless, the chlorite-rich fault rocks forms at extreme fluid/rock ratios (Teagle and Alt, 2004) (Fig. 10).

Titanium and aluminium are traditionally assumed to be immobile during hydrothermal alteration (e.g. MacLean and Barrett, 1993), but these elements display slight mobility in all three of the altered rock types. Titanium shows changes in the range of slightly more than ± 10% which is consistent with the formation of secondary titanite in the

chlorite fault rock. Despite the localized formation of secondary titanite, the fault rocks have lost titanium compared to fresh layered gabbro (median = −14%). Alumina is slightly to moderately depleted. This loss of alumina may relate to the strong losses of calcium for all three rock types and a gain of sodium for hanging and footwall samples as well as clasts, due to the partial albitisation of plagioclase (Figs. 6, 10 & supplementary Fig. A9\_2). The chlorite-rich fault rocks have lost >90% of calcium compared to fresh layered gabbro reflecting the complete breakdown of plagioclase, with only minor epidote present. Iron and manganese are moderately to highly depleted in hanging and footwall rocks and clasts respectively, whereas the chlorite-rich fault rocks are highly enriched in both elements (Figs. 10 & supplementary Fig. A9\_2). The high iron concentrations mainly reflect hydrothermal sulphide mineralisation and their subsequent iron oxyhydroxide weathering products, respectively.

The most significant feature of all three rock types is the large increase of volatiles, as seen in an increase of loss on ignition (L.O.I.) when compared to fresh layered gabbro. This increase mainly reflects hydration during fluid-rock interaction with only minor carbonation. The hanging and footwall samples as well as clast sample AH6 have only minor calcium carbonates present in small veins. Consequently, most of the increase in L.O.I. is due to the formation of hydrous hydrothermal minerals such as chlorite, amphibole, prehnite and laumontite. Hanging wall sample OM15-3A shows a considerable gain of volatiles, reflecting high modal abundances of laumontite and prehnite. For clast sample AH7 and all the fault rock samples the increase of L.O.I. is mainly due to high abundances of chlorite (± minor epidote).

Even though Y, Zr and Hf are generally considered as immobile elements during hydrothermal processes (MacLean and Barrett, 1993; MacLean and Kranidiotis, 1987), they show considerable mass gains in all three rock types. Fresh layered gabbros and altered samples have low concentrations of Zr (−3–15 µg/g) and Y (−4–13 µg/g), and consequently, minor variations in concentration can result in considerable



relative mass gains or losses. However, mobility of high-field strength elements (HFSE) in hydrothermal systems and hydrothermal zircons have been reported from MOR settings (e.g. Augustin et al., 2008).

In general, the alkali elements are very sensitive tracers of hydrothermal activity. Lithium is depleted in all three rock types, up to 50% in hanging and footwall and clasts but slightly less so in the chlorite-rich fault rocks (Fig. 10). Lithium is known to be highly mobile during hydrothermal processes in oceanic crust: low-temperature processes lead to an increase in Li concentration in host rocks but, Li is significantly mobilised by hydrothermal processes at greenschist to sub-amphibolite facies conditions (Chan et al., 2002). Interestingly, Li is less depleted in the chlorite-rich fault rock compared to the other two rock types, despite the higher alteration degree. This may be explained by the substitution of Li for Mg, due to their similar ionic radii (~0.76 Å), and the high abundance of Mg-chlorite in these rocks. Both, Rb and Cs are depleted in all three rock types (Fig. 10), suggesting they were leached and lost to the hydrothermal fluid. From black smoker systems it is well known that Rb and Cs are leached almost completely during intensive fluid-rock interaction at temperatures ~350 °C leading to Rb and Cs concentrations of black smoker fluids nearly as high as measured in basalts (Palmer and Edmond, 1989; Von Damm, 1995). Sr and Ba have an affinity for Ca, and Sr is predominantly incorporated in secondary minerals such as secondary plagioclase, prehnite and laumontite in hanging wall and footwall and is therefore gained. Even though Sr substitutes for Ca of epidote in the fault rock, it cannot counterbalance the loss of Sr due to the decay of plagioclase and therefore Sr is highly depleted in the fault rock. Ba is enriched in both the wall samples and the clasts and slightly enriched in the fault rock, although the range in the fault rock is large.

Sc, V, Cr, Ni and Pb are all depleted in hanging and footwall, clasts and the fault rock, whereas Co, Cu and Zn are depleted in hanging and footwall but present in high concentrations in the chlorite-rich fault rocks, reflecting sulphide mineralisation and their weathering products (Fig. 10). Although clast sample AH6 shows similar behaviour to the hanging and footwall samples, the more altered sample AH7 has elevated Cu and Zn concentrations, reflecting the presence of sulphides. Mass change calculations indicate that Co, Zn, and Cu are leached out of the precursor rock during intensive hydrothermal fluid-rock interaction and precipitated locally in the fault rock. Presumably, this alteration occurred at relatively high temperatures (~350 °C), where the solubility of metals in hydrothermal fluids is significantly increased (Seewald and Seyfried,

1990). Such a metal depletion during hydrothermal alteration has been observed in other oceanic and ophiolitic crustal sections, from both the lower and the upper crust (Alt et al., 2010; Coggon et al., 2016; Coogan et al., 2006; Heft et al., 2008; Humphris et al., 1998; Nehlig et al., 1994).

For all three alteration types the behaviour of the LREE (La-Sm) is decoupled from the HREE (Gd-Lu). The HREE have been assumed to be immobile and were used to normalize mass changes. In contrast, the LREE are depleted in most samples when compared to fresh layered gabbro, with La being most depleted. A pronounced negative Eu anomaly is common to all altered rock types (Fig. 10) and is presumably related to both, albitisation of plagioclase (Klinkhammer et al., 1994) and fluid chemistry coupled with specific pressure and T conditions (Beermann et al., 2017). This is most extreme in the chlorite-rich fault rocks, where plagioclase is completely dissolved and replaced, leading to a release of Eu into the hydrothermal fluid. In contrast, there are three samples (AD5, AD7 and OM15-3E) that display gains of LREE and a less pronounced negative Eu anomalies (supplementary Fig. A9). This reflects the presence of open-space filling epidote in these samples that appear to have precipitated directly from the hydrothermal fluid rather than as a replacement of primary igneous minerals. Hydrothermal epidote tends to show flat to slightly LREE-enriched patterns, with a pronounced positive Eu anomaly (Gillis et al., 1992).

U is generally highly enriched in all three rock types (Fig. 10) whereas it shows low abundances in fresh layered gabbro. Previous studies from the upper oceanic crust have shown that U is enriched during low-temperature (<100 °C) hydrothermal process (Bloch, 1980; Hart and Staudigel, 1982), although Bach et al. (2003) suggest that U uptake continues under lower greenschist facies conditions. Ba is enriched in all three rock types, indicating an uptake during hydrothermal alteration.

### 8.3. The effect of weathering

Some of the samples are not only affected by hydrothermal alteration but also show signs of weathering (e.g. formation of oxyhydroxides, carbonates). Especially some of the fault rock samples (DT-10 and OM15-3C) show high contents of CO<sub>2</sub> and H<sub>2</sub>O-bearing weathering minerals such as calcite, malachite and Fe-hydroxide. Such weathering minerals also contribute to the high observed gain of volatiles. Moreover, Fe-oxyhydroxides are proposed to host or adsorb U

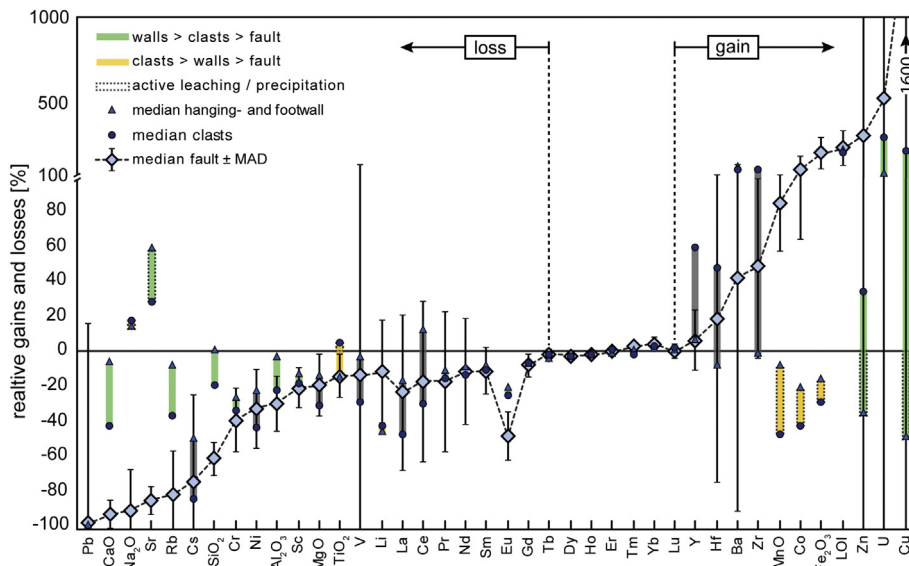


Fig. 10. Major- and trace element gains and losses for all three rock types shown relative to the median value of fresh background layered gabbro (n = 8). Elements are ranked by highest loss (left-hand side) to highest gain (right-hand side) plotted for the median fault rock. Note change in scale for gains greater than 100%.

(Bach et al., 2003; Staudigel et al., 1996; Teagle et al., 1996), indicating that U uptake might extend to the surface weathering processes.

Additionally, calcite from laumontite-calcite veins shows the most radiogenic compositions, close to present day groundwater observed in gabbro hosted wells in Wadi Tayin and within the range of Miocene sediments that once covered the ophiolite. This indicates that calcite is likely to have formed later in the history of the ophiolite and is not necessarily related to the ocean ridge hydrothermal circulation and alteration previously described.

#### 8.4. Importance of lower crustal fault zone for global elemental fluxes

To assess the hydrothermal contribution of fault zones similar to the feature described above to global geochemical cycles, we have converted our estimated hydrothermal mass changes to net elemental fluxes into or from the lower crust. Given our field observations and aerial photograph observations on the occurrence of these altered zones (Coogan et al., 2006), we assume that similar faults are spaced every 1000 m perpendicular to the ridge axis and continue along strike for 500 m, such that there is one fault zone per square kilometre of seafloor. The modelled fault zones comprise 0.6 m of fault rock and 0.4 m of clasts, flanked by a 30 m wide alteration halo (total width, including hanging wall and footwall) and cut through 4000 m of gabbro (Fig. 11). The net mass flux ( $F_i$ ) of component  $i$  through  $1 \text{ km}^2$  of seafloor due to lower crustal faulting is therefore given by:

$$F_i = \sum_z^{FZ} V_z \rho_z \Delta m_{i-z}$$

where  $\Delta m_{i-z}$  is the average change in mass of component  $i$  per kilogram of rock in each sub-zone ( $z$ ) of the fault zone (FZ),  $V_z$  is the volume of each sub-zone (fault rock =  $1.2 \times 10^6 \text{ m}^3$ , clasts =  $0.8 \times 10^6 \text{ m}^3$ , halo =  $100 \times 10^6 \text{ m}^3$ ) and  $\rho_z$  is the density of each sub-zone (assumed to be 3100, 2700 and 2800  $\text{kg/m}^3$ , for the fault rock, clasts and halo respectively). Sources of uncertainty in the calculated values of  $F_i$  will include (i) geochemical analytical uncertainty; (ii) uncertainty in calculated hydrothermal mass changes, for example reflecting the choice of precursor composition, the assumptions regarding element immobility, and the compositional variability within each altered sub-zone of the fault;

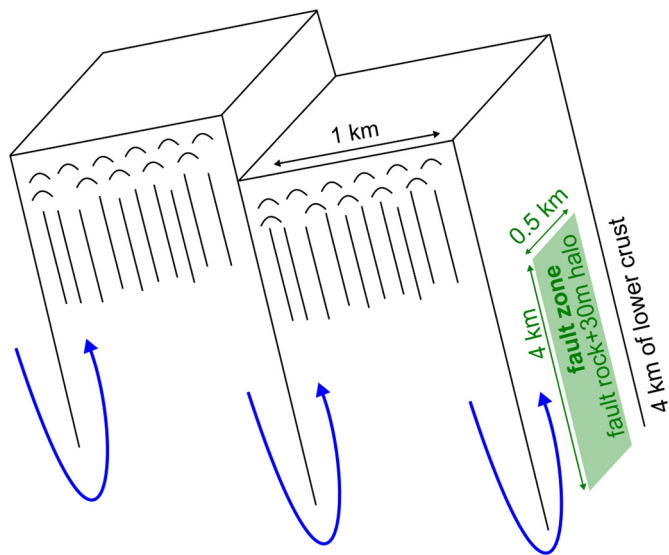


**Fig. 11.** Schematic sketch showing the model set up of one fault zone (0.6 m of fault rock + 0.4 m of clasts with a total alteration halo of 30 m) in one block of lower crust (1 km × 1 km × 4 km). The ridge-parallel fault zone continues for 500 m and faults are spaced every 1 km perpendicular to the ridge axis.

and (iii) uncertainty in fault geometry and spacing, and hence the modelled volumes of fault sub-zones ( $V_z$ ). A full propagation of these errors is beyond the scope of this paper. Here the net elemental mass fluxes ( $F_i$ ) due to lower crustal faulting are therefore determined from the median calculated chemical changes for each sub-zone of the fault (see Section 8.2.2), with the uncertainty propagated from the median absolute deviation of the calculated chemical changes for each rock type, as compositional variability of the altered rocks is expected to be the dominant source of uncertainty. The impact of uncertainty in fault geometry/spacing is discussed below (Fig. 11).

To assess the importance of such fault zones to global hydrothermal budgets, we compare our calculated hydrothermal fluxes due to lower crustal faulting with published estimates of the hydrothermal fluxes associated with the pervasive 'background' alteration of ocean crust determined from analyses of: (i) a full section of 10 Ma ocean crust sub-aerially exposed in the sub-Antarctic Macquarie Island ophiolite (Coggon et al., 2016); and (ii) samples of ocean crust recovered from several sites by scientific ocean drilling, that were combined to yield a composite full-crustal section (Staudigel, 2014; Table 3). The 2.7 km thick Macquarie crustal section includes lavas, a mineralised lava-dike transition zone, sheeted dikes, and 1 km of lower crustal gabbros produced at a slow spreading rate (10 mm/yr half rate). The hydrothermal fluxes of the composite section were predominantly determined from analyses of 120 Ma slow-spread lavas and 9 Ma ultra-slow spread gabbros. Note that there are significant discrepancies between the results of these two studies, which likely reflect both global variations in the nature and extent of hydrothermal alteration and the differing methods used to calculate the hydrothermal fluxes (see discussion in Coggon et al., 2016). Here we consider lower crustal hydrothermal faulting to make a significant contribution to global hydrothermal budgets for a given element if the magnitude of our calculated flux is >10% of the hydrothermal flux in to or from either the Macquarie crust or the composite crustal section (Table 3). Our results indicate that given our assumed fault spacing and geometry, lower crustal faults contribute significantly to the global hydrothermal budgets of Si, Ti, Al, Fe, Mn, Mg, Ca, H<sub>2</sub>O, Cu, Zn, Sr and Cs (Fig. 12; Table 3).

Assuming that hydration is the main cause of volatile enrichment within the sampled fault zones, our results indicate that the previously undocumented additional water-uptake during lower crustal faulting is equivalent to 20% of the total water-uptake during background alteration of ocean crust (Coggon et al., 2016; Staudigel, 2014).

For elements such as Ca, Al, Fe, Na, Zn and Sr, where the change (compared to Macquarie crust) is in the same sense, our results clearly indicate a significant previously unquantified flux. For other elements such as Si or Cu, where the change (compared to Macquarie crust) is not the same sense and elements previously were assumed to leave the crust, it may be that they are partially remobilized into the fault zones.

Here we have shown that if the lower crustal faulting observed within the Semail ophiolite is globally representative of faulting within lower ocean crust, then such fault zones contribute significantly to the global hydrothermal budgets for many elements. Furthermore, if we have underestimated the spacing of lower crustal fault zones [e.g. fault spacing of only a few hundred metres observed at the East Pacific Rise (Bicknell et al., 1987; Bohnenstiehl and Carbotte, 2001; Edwards et al., 1991)], and/or the width of the fault zone alteration halo (the dominant mass-fraction of the fault zone), then their contribution to global hydrothermal fluxes is even more significant.

## 9. Conclusions

Secondary mineral assemblages, major- and trace element mass change calculations and strontium isotope compositions suggest that this chlorite-rich fault zone represents a fossilized discharge zone of hot, upwelling hydrothermal fluids with Sr-isotopic compositions in the range  $^{87}\text{Sr}/^{86}\text{Sr} = 0.7043\text{--}0.7048$ , similar to epidote present in

**Table 3**

Comparison of estimated hydrothermal net fluxes in (+) and out (-) of the lower oceanic crust due to faulting in comparison with extrapolated global hydrothermal from Macquarie island ophiolite (Coggon et al., 2016) and a composite section (Staudigel, 2014). Significant fluxes (magnitude at least 10% of background hydrothermal flux) are highlighted in light green.

Total flux Fault zone	Macquarie Island		Composite
	median	range	ophiolite <sup>a)</sup>
			section ODP <sup>b)</sup>
<b>Major elements</b>			
	10 <sup>12</sup> mol/year	10 <sup>12</sup> mol/year	10 <sup>12</sup> mol/year
<b>Si</b>	0.0540	-0.86 to 0.97	-1.17 to 0.33
<b>Ti</b>	-0.0386	-0.039 to -0.038	-0.25 to -0.08
<b>Al</b>	-0.1610	-0.79 to 0.47	-1.94 to 0.10
<b>Fe</b>	-0.1130	-0.24 to 0.013	-0.28 to 0.66
<b>Mn</b>	-0.0012	-0.0034 to 0.0011	-0.01 to 0.01
<b>Mg</b>	-0.503	-0.85 to -0.15	2.26 to 4.35
<b>Ca</b>	-0.287	-0.569 to -0.0045	-5.48 to -4.16
<b>Na</b>	0.06	-0.047 to 0.17	1.79 to 2.81
<b>H<sub>2</sub>O</b>	3.9400	2.75 to 5.13	17.6 to 19.8
<b>Trace elements</b>			
	10 <sup>8</sup> mol/year	10 <sup>8</sup> mol/year	10 <sup>8</sup> mol/year
<b>Cu</b>	-6.690	-41.9 to 28.9	-78 to -51
<b>Zn</b>	-1.400	-2.3 to -0.48	-12 to -1.0
<b>Rb</b>	-0.001	-0.004 to 0.002	- 1.2 to 2.2
<b>Sr</b>	13.0	7.48 to 18.4	- 7.1 to 22
<b>Cs</b>	-0.0003	-0.0003 to -0.0002	- 0.005 to 0.04
<b>Ba</b>	0.368	0.297 to 0.439	3.8 to 22
<b>U</b>	0.00045	-0.0007 to 0.002	-0.03 to -0.01

<sup>a</sup>Coggon et al., 2016.

<sup>b</sup>After Staudigel (2014).

hydrothermal veins in the Samail ophiolite. Chlorite thermometry indicates formation temperatures of 300–350 °C for the fault rock and calculations based on silica solubility in hydrothermal fluids give an estimate of high fluid/rock ratios of 450:1–900:1. Due to intensive fluid-rock interaction elements were mobilized and locally redistributed. Ca, Na, Si, Al, Mg, Mn, Fe, Ti as well as Pb, Rb, Cs, Cr, Ni, Sc, V, Cu, LREE, Co, Zn and Li were leached and either transported away by the passage of hydrothermal fluids or were partially incorporated into secondary phases such as chalcopyrite and pyrite (Fe, Cu, Zn, Co) or epidote (LREE) in the fault rock itself or into secondary phases such as plagioclase, prehnite and laumontite (Na, Sr) in the wall rocks. H<sub>2</sub>O and other elements such as Ba, U were transported with the hydrothermal fluid and scavenged within the system. Intense exchange of the hydrothermal fluid with the rock is limited to between 1m and 30 m from the fault zone,

as evidenced by the alteration around the fault zone observed in the field. Our results suggest that hydrothermal fluids reach deep into the lower plutonic oceanic crust and, hence, provide an efficient cooling system being the prerequisite for in situ crystallization and accretion as proposed in the sheeted sills model.

From calculated mass changes we estimated global hydrothermal fluxes for one lower crustal fault zone per one cube of lower oceanic crust (1 km × 1 km × 4 km), assuming a crustal production rate of 5 km<sup>2</sup>/y. Our results indicate that given the assumed fault spacing and geometry, lower crustal faults contribute significantly to the global hydrothermal budgets of Si, Ti, Al, Fe, Mn, Mg, Ca, H<sub>2</sub>O, Cu, Zn, Sr and Cs.

Supplementary data to this article can be found online at <https://doi.org/10.1016/j.lithos.2018.09.008>.

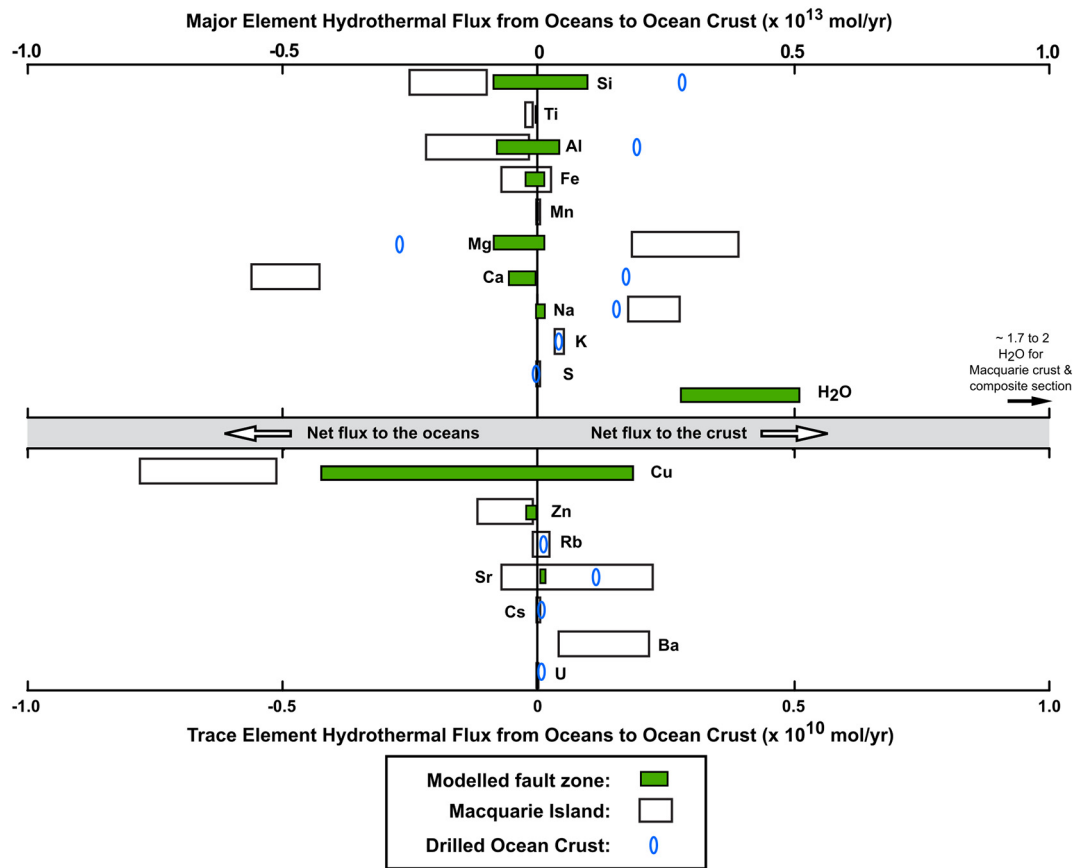


**Fig. 12.** Hydrothermal fluxes (mol/yr) extrapolated from estimated mass changes occurring during hydrothermal alteration in a lower crustal fault (green bars). In comparison hydrothermal fluxes calculated from pervasive hydrothermal background alteration for Macquarie Island ophiolite (white bars; Coggon et al., 2016) and a composite crustal section recovered by scientific ocean drilling (blue ovals; Staudigel, 2014). Diagram modified after Coggon et al. (2016). Fluxes for Ti, Mn, Cs, Ba and U are too small to be shown in this diagram.

## Acknowledgements

We greatly acknowledge reviews from A. Barker and an anonymous reviewer that helped to improve this manuscript. T. Müller is thanked for providing  $^{87}\text{Sr}/^{86}\text{Sr}$  measurements of eight fresh layered gabbro samples. We thank M. Cooper, U. Westernströer, and K. Bremer for their assistance in the laboratories, A. Barker and L. Crispini for helpful thin section discussions, M. Schori and O. Beermann for fieldwork assistance and M. Harris for providing an early version of Fig. 11. We thank the Public Authority for Mining of the Sultanate of Oman for allowing us to conduct field work. The research leading to these results received funding from the People Programme (Marie Curie Actions) of the European Union's Seventh Framework Programme FP7/2007–2013 under the REA grant agreement no. 608001, that supported BZ within the “Abyss” Initial Training Network. DT is supported by a Royal Society Wolfson Research Merit Award (WM130051). Further essential funding was contributed to DGS by Deutsche Forschungsgemeinschaft (DFG, German Research Foundation) under grant No. 398945252 and to JK by Deutsche Forschungsgemeinschaft (DFG, German Research Foundation) under grant No. 270849521.

## References

- Alabaster, T., Pearce, J.A., Malpas, J., 1982. The volcanic stratigraphy and petrogenesis of the Oman ophiolite complex. *Contrib. Mineral. Petrol.* 81, 168–183.
- Alt, J.C., Laverne, C., Coggon, R.M., Teagle, D.A.H., Banerjee, N.R., Morgan, S., Smith-Duque, C.E., Harris, M., Galli, L., 2010. Subsurface structure of a submarine hydrothermal system in ocean crust formed at the East Pacific Rise, ODP/IODP Site 1256. *Geochem. Geophys. Geosyst.* 11, 1–28. <https://doi.org/10.1029/2010GC003144>.
- Augustin, N., Lackschewitz, K.S., Kuhn, T., Devey, C.W., 2008. Mineralogical and chemical mass changes in mafic and ultramafic rocks from the Logatchev hydrothermal field (MAR 15 N). *Mar. Geol.* 256, 18–29.
- Bach, W., Bernhard, P.E., Hart, S.R., Blusztajn, J.S., 2003. Geochemistry of hydrothermally altered oceanic crust: DSDP/ODP Hole 504B—Implications for seawater–crust exchange budgets and Sr- and Pb-isotopic evolution of the mantle. *Geochem. Geophys. Geosyst.* 4, 40–55. <https://doi.org/10.1029/2002GC000419>.
- Beermann, O., Garbe-Schönberg, D., Bach, W., Holzheid, A., 2017. Time-resolved interaction of seawater with gabbro: an experimental study of rare-earth element behavior up to 475 °C, 100 MPa. *Geochim. Cosmochim. Acta* 197, 167–192.
- Bickle, M.J., Teagle, D.A.H., 1992. Strontium alteration in the Troodos ophiolite: implications for fluid fluxes and geochemical transport in mid-ocean ridge hydrothermal systems. *Earth Planet. Sci. Lett.* 113, 219–237.
- Bicknell, J.D., Sempere, J.-C., Macdonald, K.C., Fox, P.J., 1987. Tectonics of a fast spreading center: a deep-tow and sea beam survey on the East Pacific Rise at 19° 30' S. *Mar. Geophys. Res.* 9, 25–45.
- Bloch, S., 1980. Some factors controlling the concentration of uranium in the world ocean. *Geochim. Cosmochim. Acta* 44, 373–377.
- Bohnenstiehl, D.R., Carbotte, S.M., 2001. Faulting patterns near 19° 30' S on the East Pacific Rise: Fault formation and growth at a superfast spreading center. *Geochem. Geophys. Geosyst.* 2.
- Bosch, D., Jamais, M., Boudier, F., Nicolas, A., Dautria, J.M., Agrinier, P., 2004. Deep and high-temperature hydrothermal circulation in the Oman ophiolite - Petrological and isotopic evidence. *J. Petrol.* 45, 1181–1208.
- Boudier, F., Nicolas, A., 2007. Comment on “dating the geologic history of Oman’s Semail ophiolite: Insights from U–Pb geochronology” by C. J. Warren, R. R. Parrish, D. J. Waters and M. P. Searle. *Contributions to Mineralogy and Petrology* 154, 111–113. <https://doi.org/10.1007/s00410-007-0189-5>
- Boudier, F., Nicolas, A., Ildefonse, B., 1996. Magma chambers in the Oman ophiolite: fed from the top and the bottom. *Earth Planet. Sci. Lett.* 144, 239–250.
- Browning, P., 1984. Cryptic variation within the cumulate sequence of the Oman ophiolite: magma chamber depth and petrological implications. *Geol. Soc. Lond., Spec. Publ.* 13, 71–82.
- Cathelineau, M., 1988. Cation site occupancy in chlorites and illites as function of temperature. *Clay Miner.* 23, 471–485.
- Cathelineau, M., Nieva, D., 1985. A chlorite solid solution geothermometer. The Los Azufres (Mexico) geothermal system. *Contrib. Mineral. Petrol.* 91, 235–244.

- Chan, L.H., Alt, J.C., Teagle, D.A.H., 2002. Lithium and lithium isotope profiles through the upper oceanic crust: a study of seawater-basalt exchange at ODP Sites 504B and 896A. *Earth Planet. Sci. Lett.* 201, 187–201. [https://doi.org/10.1016/S0012-821X\(02\)00707-0](https://doi.org/10.1016/S0012-821X(02)00707-0).
- Chen, Y.J., 2001. Thermal effects of gabbro accretion from a deeper second melt lens at the fast spreading East Pacific Rise. *J. Geophys. Res. Solid Earth* 106, 8581–8588.
- Coggon, R.M., Teagle, D.A.H., Harris, M., Davidson, G.J., Alt, J.C., Brewer, T.S., 2016. Hydrothermal contributions to global biogeochemical cycles: insights from the Macquarie Island ophiolite. *Lithos* 264, 329–347.
- Coogan, L.A., Howard, K.A., Gillis, K.M., Bickle, M.J., Chapman, H., Boyce, A.J., Jenkin, G.R.T., Wilson, R.N., 2006. Chemical and thermal constraints on focussed fluid flow in the lower oceanic crust. *Am. J. Sci.* 306, 389–427.
- Coogan, L.A., Jenkin, G.R.T., Wilson, R.N., 2002. Constraining the cooling rate of the lower oceanic crust: a new approach applied to the Oman ophiolite. *Earth Planet. Sci. Lett.* 199, 127–146.
- Coogan, L.A., Manning, C.E., Wilson, R.N., 2007. Oxygen isotope evidence for short-lived high-temperature fluid flow in the lower oceanic crust at fast-spreading ridges. *Earth Planet. Sci. Lett.* 260, 524–536.
- Edwards, M.H., Fornari, D.J., Malinverno, A., Ryan, W.B.F., Madsen, J., 1991. The regional tectonic fabric of the East Pacific Rise from 12° 50' N to 15° 10' N. *J. Geophys. Res. Solid Earth* 96, 7995–8017.
- Faak, K., Coogan, L.A., Chakraborty, S., 2015. Near conductive cooling rates in the upper-plutonic section of crust formed at the East Pacific Rise. *Earth Planet. Sci. Lett.* 423, 36–47.
- Faak, K., Gillis, K.M., 2016. Slow cooling of the lowermost oceanic crust at the fast-spreading East Pacific Rise. *Geology* 44, 115–118.
- France, L., Ildefonse, B., Koepke, J., 2009. Interactions between magma and hydrothermal system in Oman ophiolite and in IODP Hole 1256D: fossilization of a dynamic melt lens at fast spreading ridges. *Geochem. Geophys. Geosyst.* 10, 1–30. <https://doi.org/10.1029/2009GC002652>.
- Garbe-Schönberg, C.D., 1993. Simultaneous determination of thirty-seven trace elements in twenty-eight international rock standards by ICP-MS. *Geostand. Newslett.* 17, 81–97.
- Garbe-Schönberg, D., Müller, S., 2014. Nano-particulate pressed powder tablets for LA-ICP-MS. *J. Anal. At. Spectrom.* 29, 990–1000.
- Gillis, K.M., Ludden, J.N., Smith, A.D., 1992. Mobilization of REE during crustal aging in the Troodos Ophiolite, Cyprus. *Chem. Geol.* 98, 71–86.
- Gillis, K.M., Snow, J.E., Klaus, A., Abe, N., Adriaño, Á.B., Akizawa, N., Ceuleneer, G., Cheadle, M.J., Faak, K., Falloun, T.J., Friedman, S.A., Godard, M., Guerin, G., Harigane, Y., Horst, A.J., Hoshida, T., Ildefonse, B., Jean, M.M., John, B.E., Koepke, J., MacHi, S., Maeda, J., Marks, N.E., McCaig, A.M., Meyer, R., Morris, A., Nozaka, T., Python, M., Saha, A., Wintsch, R.P., 2014. Primitive layered gabbros from fast-spreading lower oceanic crust. *Nature* 505, 204–207. <https://doi.org/10.1038/nature12778>.
- Godard, M., Dautria, J.M., Perrin, M., 2003. Geochemical variability of the Oman ophiolite lavas: Relationship with spatial distribution and paleomagnetic directions. *Geochem. Geophys. Geosyst.* 4. <https://doi.org/10.1029/2002GC000452>.
- Goodenough, K.M., Thomas, R.J., Styles, M.T., Schofield, D.I., MacLeod, C.J., 2014. Records of ocean growth and destruction in the Oman-UAE ophiolite. *Elements* 10, 109–114. <https://doi.org/10.2113/gselements.10.2.109>.
- Grant, J.A., 1986. The isocon diagram; a simple solution to Gresens equation for metasomatic alteration. *Econ. Geol.* 81, 1976–1982.
- Gregory, R.T., Taylor, H.P., 1981. An oxygen isotope profile in a section of Cretaceous oceanic crust, Samail Ophiolite, Oman: evidence for  $\delta^{18}\text{O}$  buffering of the oceans by deep (>5 km) seawater-hydrothermal circulation at mid-ocean ridges. *J. Geophys. Res. Solid Earth* 86, 2737–2755.
- Gresens, R.L., 1967. Composition - volume relationships of metasomatism. *Chem. Geol.* 2, 47–65.
- Haase, K.M., Freund, S., Beier, C., Koepke, J., Erdmann, M., Häuff, F., 2016. Constraints on the magmatic evolution of the oceanic crust from plagiogranite intrusions in the Oman ophiolite. *Contrib. Mineral. Petrol.* 171, 46.
- Harris, M., Coggon, R.M., Smith-Duque, C.E., Cooper, M.J., Milton, J.A., Teagle, D.A.H., 2015. Channelling of hydrothermal fluids during the accretion and evolution of the upper oceanic crust: Sr isotope evidence from ODP Hole 1256D. *Earth Planet. Sci. Lett.* 416, 56–66. <https://doi.org/10.1016/j.epsl.2015.01.042>.
- Hart, S.R., Staudigel, H., 1982. The control of alkalies and uranium in seawater by ocean crust alteration. *Earth Planet. Sci. Lett.* 58, 202–212. [https://doi.org/10.1016/0012-821X\(82\)90194-7](https://doi.org/10.1016/0012-821X(82)90194-7).
- Hasenclever, J., Theissen-Krah, S., Rüpke, L.H., Morgan, J.P., Iyer, K., Petersen, S., Devey, C.W., 2014. Hybrid shallow on-axis and deep off-axis hydrothermal circulation at fast-spreading ridges. *Nature* 508, 508–512. <https://doi.org/10.1038/nature13174>.
- Heft, K.L., Gillis, K.M., Pollock, M.A., Karson, J.A., Klein, E.M., 2008. Role of upwelling hydrothermal fluids in the development of alteration patterns at fast spreading ridges: evidence from the sheeted dike complex at Pito Deep. *Geochem. Geophys. Geosyst.* 9. <https://doi.org/10.1029/2007GC001926>.
- Henstock, T.J., Woods, A.W., White, R.S., 1993. The accretion of oceanic crust by episodic sill intrusion. *J. Geophys. Res. Solid Earth* 98, 4143–4161.
- Hopson, C.A., Coleman, R.G., Gregory, R.T., Pallister, J.S., Bailey, E.H., 1981. Geologic section through the Samail Ophiolite and associated rocks along a Muscat-Ibra Transect, southeastern Oman Mountains. *J. Geophys. Res.* 86, 2527. <https://doi.org/10.1029/JB086iB04p02527>.
- Humphris, S.E., Alt, J.C., Teagle, D.A.H., Honnorez, J.J., 1998. Geochemical changes during hydrothermal alteration of basement in the stockwork beneath the active TAG hydrothermal mound. *Proceedings Ocean Drilling Program Scientific Results*. National Science Foundation, pp. 255–276.
- Jowett, E.C., 1991. Fitting iron and magnesium into the hydrothermal chlorite geothermometer. *GAC/MAC/SEG Joint Annual Meeting*, Toronto, May 27–29, 1991, Program with Abstracts 16.
- Kelemen, P.B., Koga, K., Shimizu, N., 1997. Geochemistry of gabbro sills in the crust-mantle transition zone of the Oman ophiolite: implications for the origin of the oceanic lower crust. *Earth Planet. Sci. Lett.* 146, 475–488. [https://doi.org/10.1016/S0012-821X\(96\)00235-X](https://doi.org/10.1016/S0012-821X(96)00235-X).
- Klinkhammer, G.P., Elderfield, H., Edmond, J.M., Mitra, A., 1994. Geochemical implications of rare earth elements patterns in hydrothermal fluids from mid-ocean ridges. *Geochem. Cosmochim. Acta* 58, 5105–5113.
- Koepke, J., Schoenborn, S., Oelze, M., Wittmann, H., Feig, S.T., Hellebrand, E., Boudier, F., Schoenberg, R., 2009. Petrogenesis of crustal wehrlites in the Oman ophiolite: experiments and natural rocks. *Geochem. Geophys. Geosyst.* 10.
- Kranidiotis, P., MacLean, W.H., 1987. Systematics of chlorite alteration at the Phelps Dodge massive sulfide deposit, Matagami, Quebec. *Econ. Geol.* 82, 1898–1911.
- Lanphere, M.A., Coleman, R.G., Hopson, C.A., 1981. Sr isotopic tracer study of the Samail Ophiolite, Oman. *J. Geophys. Res. Solid Earth* 86, 2709–2720. <https://doi.org/10.1029/JB086iB04p02709>.
- Leake, B.E., Woolley, A.R., Arps, C.E.S., Birch, W.D., Gilbert, M.C., Grice, J.D., Hawthorne, F.C., Kato, A., Kisch, H.J., Krivovichev, V.G., Linthouk, K., 1997. Report. nomenclature of amphiboles: report of the subcommittee on amphiboles of the International Mineralogical Association Commission on new minerals and mineral names. *Mineral. Mag.* 61, 295–321.
- MacLean, W.H., 1990. Mass change calculations in altered rock series. *Mineral. Deposita* 25, 44–49.
- MacLean, W.H., Barrett, T.J., 1993. Lithochemical techniques using immobile elements. *J. Geochem. Explor.* 48, 109–133.
- MacLean, W.H., Kranidiotis, P., 1987. Immobile elements as monitors of mass transfer in hydrothermal alteration; Phelps Dodge massive sulfide deposit, Matagami, Quebec. *Econ. Geol.* 82, 951–962.
- MacLennan, J., Hulme, T., Singh, S.C., 2004. Thermal models of oceanic crustal accretion: linking geophysical, geological and petrological observations. *Geochem. Geophys. Geosyst.* 5. <https://doi.org/10.1029/2003GC000605>.
- MacLeod, C.J., Lissenberg, C.J., Bibby, L.E., 2013. “Moist MORB” axial magmatism in the Oman ophiolite: the evidence against a mid-ocean ridge origin. *Geology* 41, 459–462.
- MacLeod, C.J., Yaouancq, G., 2000. A fossil melt lens in the Oman ophiolite: implications for magma chamber processes at fast spreading ridges. *Earth Planet. Sci. Lett.* 176, 357–373.
- Manning, C.E., MacLeod, C.J., Weston, P.E., 2000. Lower-crustal cracking front at fast-spreading ridges: evidence from the East Pacific Rise and the Oman ophiolite. *Special Papers-Geological Society of America*, pp. 261–272.
- Manning, C.E., Weston, P.E., Mahon, K.L., 1996. Rapid high-temperature metamorphism of East Pacific Rise gabbros from Hess Deep. *Earth Planet. Sci. Lett.* 144, 123–132.
- McArthur, J.M., Howarth, R.J., Bailey, T.R., 2001. Strontium isotope stratigraphy: LOWESS version 3: best fit to the marine Sr-isotope curve for 0–509 Ma and accompanying look-up table for deriving numerical age. *J. Geol.* 109, 155–170.
- McCulloch, M.T., Gregory, R.T., Wasserburg, G.J., Taylor, H.P., 1981. Sm-Nd, Rb-Sr, and  $^{18}\text{O}/^{16}\text{O}$  isotopic systematics in an oceanic crustal section: evidence from the Samail Ophiolite. *J. Geophys. Res. Solid Earth* 86, 2721–2735.
- McCulloch, M.T., Gregory, R.T., Wasserburg, G.J., Taylor, H.P., 1980. A Neodymium, Strontium, and Oxygen Isotopic Study of the cretaceous Samail ophiolite and implications for the petrogenesis and seawater-hydrothermal alteration of oceanic crust. *Earth Planet. Sci. Lett.* 46, 201–211.
- McDonough, William F., Sun, S.-S., 1995. The composition of the Earth. *Chemical geology* 120 (3–4), 223–253.
- McDowell, S.D., Elders, W.A., 1980. Authigenic layer silicate minerals in borehole Elmore 1, Salton Sea geothermal field, California, USA. *Contributions to Mineralogy and Petrology*, vol. 74, pp. 293–310.
- Morgan, J.P., Chen, Y.J., 1993. The genesis of oceanic crust: magma injection, hydrothermal circulation, and crustal flow. *J. Geophys. Res. Solid Earth* 98, 6283–6297.
- Morton, J.L., Sleep, N.H., 1985. A mid-ocean ridge thermal model: constraints on the volume of axial hydrothermal heat flux. *J. Geophys. Res. Solid Earth* 90, 11345–11353.
- Mueller, S., Koepke, J., Garbe-Schoenberg, C.D., Müller, T., Mock, D., Strauss, H., Schuth, S., Ildefonse, B., 2017. A reference section through the lower fast-spreading oceanic crust in the Wadi Gideah (Samail ophiolite, Sultanate Oman): drill sites GT1A and GT2A within the ICDP Oman Drilling Project. *AGU Fall Meeting Abstracts*.
- Müller, T., 2016. A Petrological and Geochemical Cross Section of Lower Crust at the Wadi Gideah (Samail ophiolite): Implications for the Crustal Accretion at Fast-Spreading Mid-Ocean Ridges (PhD thesis). *Gottfried Wilhelm Leibniz Universität Hannover, Géosciences Montpellier Université Montpellier*.
- Müller, T., Koepke, J., Garbe-Schönberg, C.-D., Dietrich, M., Bauer, U., Wolff, P.E., 2017. Anatomy of a frozen axial melt lens from a fast-spreading paleo-ridge (Wadi Gideah, Oman ophiolite). *Lithos* 272, 31–45.
- Nehlig, P., Juteau, T., 1988. Deep crustal seawater penetration and circulation at ocean ridges: evidence from the Oman ophiolite. *Mar. Geol.* 84, 209–228.
- Nehlig, P., Juteau, T., Bendel, V., Cotten, J., 1994. The root of oceanic hydrothermal systems: constraints from the Samail ophiolite (Oman). *J. Geophys. Res.* 99, 4703–4713. <https://doi.org/10.1029/93JB02663>.
- Nicolas, A., Boudier, F., Ildefonse, B., Bail, E., 2000. Accretion of Oman and United Arab Emirates ophiolite—discussion of a new structural map. *Mar. Geophys. Res.* 21, 147–180.
- Nicolas, A., Mainprice, D., Boudier, F., 2003. High-temperature seawater circulation throughout crust of oceanic ridges: a model derived from the Oman ophiolites. *J. Geophys. Res.* 108, 2371.

- Oeser, M., Strauss, H., Wolff, P.E., Koepke, J., Peters, M., Garbe-Schönberg, D., Dietrich, M., 2012. A profile of multiple sulfur isotopes through the Oman ophiolite. *Chem. Geol.* 312, 27–46.
- Pallister, J.S., 1981. Structure of the sheeted dike complex of the Samail ophiolite near Ibra, Oman. *J. Geophys. Res. Solid Earth* 86, 2661–2672.
- Pallister, J.S., Hopson, C.A., 1981. Samail ophiolite plutonic suite: field relations, phase variation, cryptic variation and layering, and a model of a spreading ridge magma chamber. *J. Geophys. Res. Solid Earth* 86, 2593–2644.
- Pallister, J.S., Knight, R.J., 1981. Rare-earth element geochemistry of the Samail Ophiolite near Ibra, Oman. *J. Geophys. Res. Solid Earth* 86, 2673–2697.
- Palmer, M.R., Edmond, J.M., 1989. Cesium and rubidium in submarine hydrothermal fluids: evidence for recycling of alkali elements. *Earth Planet. Sci. Lett.* 95, 8–14. [https://doi.org/10.1016/0012-821X\(89\)90163-5](https://doi.org/10.1016/0012-821X(89)90163-5).
- Peters, T., El Amin, O., Blechschmid, I., Al-Busaidi, S., 2008. Geological Map Oman 1:50000, Sheet NF 40-8A1. Sultanate of Oman: Ministry of Commerce and Industry.
- Peucker-Ehrenbrink, B., Hanghøj, K., Atwood, T., Kelemen, P.B., 2012. Rhenium-osmium isotope systematics and platinum group element concentrations in oceanic crust. *Geology* 40, 199–202. <https://doi.org/10.1130/G32431.1>.
- Pin, C., Briot, D., Bassin, C., Poitrasson, F., 1994. Concomitant separation of strontium and samarium-neodymium for isotopic analysis in silicate samples, based on specific extraction chromatography. *Anal. Chim. Acta* 298, 209–217.
- Quick, J.E., Denlinger, R.P., 1993. Ductile deformation and the origin of layered gabbro in ophiolites. *J. Geophys. Res. Solid Earth* 98, 14015–14027.
- Richardson, C.J., Cann, J.R., Richards, H.G., Cowan, J.G., 1987. Metal-depleted root zones of the Troodos ore-forming hydrothermal systems, Cyprus. *Earth Planet. Sci. Lett.* 84, 243–253.
- Rioux, M., Bowring, S., Kelemen, P., Gordon, S., Miller, R., Dudás, F., 2013. Tectonic development of the Samail ophiolite: High-precision U-Pb zircon geochronology and Sm-Nd isotopic constraints on crustal growth and emplacement. *J. Geophys. Res. Solid Earth* 118, 2085–2101.
- Schiffman, P., Smith, B.M., Varga, R.J., Moores, E.M., 1987. Geometry, conditions and timing of off-axis hydrothermal metamorphism and ore-deposition in the Solea graben. *Nature* 325, 423.
- Searle, M., Cox, J., 1999. Tectonic setting, origin, and obduction of the Oman ophiolite. *Geol. Soc. Am. Bull.* 111, 104–122.
- Seewald, J.S., Seyfried, W.E., 1990. The effect of temperature on metal mobility in subseafloor hydrothermal systems: constraints from basalt alteration experiments. *Earth Planet. Sci. Lett.* 101, 388–403. [https://doi.org/10.1016/0012-821X\(90\)90168-W](https://doi.org/10.1016/0012-821X(90)90168-W).
- Sleep, N.H., 1991. Hydrothermal circulation, anhydrite precipitation, and thermal structure at ridge axes. *J. Geophys. Res. Solid Earth* 96, 2375–2387.
- Staudigel, H., 2014. Chemical fluxes from hydrothermal alteration of the oceanic crust. In: Rudnick, R.L. (Ed.), *Treatise on Geochemistry, 2nd Edition The Crust Vol. 4*. Elsevier, Oxford, pp. 583–606.
- Staudigel, H., Plank, T., White, B., Schmincke, H., 1996. Geochemical fluxes during seafloor alteration of the basaltic upper oceanic crust: DSDP Sites 417 and 418. Subduction: top to bottom 96, pp. 19–38.
- Sun, C., Lissenberg, C.J., 2018. Formation of fast-spreading lower oceanic crust as revealed by a new Mg-REE coupled geospeedometer. *Earth Planet. Sci. Lett.* 487, 165–178.
- Teagle, D.A.H., Alt, J.C., 2004. Hydrothermal alteration of basalts beneath the Bent Hill massive sulfide deposit, Middle Valley, Juan de Fuca Ridge. *Econ. Geol.* 99, 561–584.
- Teagle, D.A.H., Alt, J.C., Bach, W., Halliday, A.N., Erzinger, J., 1996. Alteration of upper ocean crust in a ridge-flank hydrothermal upflow zone: mineral, chemical, and isotopic constraints from Hole 896A. *Proceedings-Ocean Drilling Program, Scientific Results*. National Science Foundation, pp. 119–150.
- Teagle, D.A.H., Bickle, M.J., Alt, J.C., 2003. Recharge flux to ocean-ridge black smoker systems: a geochemical estimate from ODP Hole 504B. *Earth Planet. Sci. Lett.* 210, 81–89.
- Theissen-Krah, S., Rüpke, L.H., Hasenclever, J., 2016. Modes of crustal accretion and their implications for hydrothermal circulation. *Geophys. Res. Lett.* 43, 1124–1131. <https://doi.org/10.1002/2015GL067335>.
- Toy, V.G., Sutherland, R., Townend, J., Allen, M.J., Becroft, L., Boles, A., Boulton, C., Carpenter, B., Cooper, A., Cox, S.C., Daube, C., Faulkner, D.R., Halfpenny, A., Kato, N., Keys, S., Kirilova, M., Kometani, Y., Little, T., Mariani, E., Melosh, B., Menzies, C.D., Morales, L., Morgan, C., Mori, H., Niemeijer, A., Norris, R., Prior, D., Sauer, K., Schleicher, A.M., Shigematsue, N., Teagle, D.A.H., Tobin, H., Valdez, R., Williams, J., Yeo, S., Baratin, L.-M., Barth, N., Benson, A., Boese, C., Célérier, B., Chamberlain, C.J., Conze, R., Coussens, J., Craw, L., Doan, M.-L., Eccles, J., Grieve, J., Grochowski, J., Gulley, A., Howarth, J., Jacobs, K., Janku-Capova, L., Jeppson, T., Langridge, R., Mallyon, D., Marx, R., Massiot, C., Mathewson, L., Moore, J., Nishikawa, O., Pooley, B., Pyne, A., Savage, M.K., Schmitt, D., Taylor-Offord, S., Upton, P., Weaver, K.C., Wiersberg, T., Zimmer, M., DFDP-2-Science Team, 2017. Bedrock geology of DFDP-2B, central Alpine Fault, New Zealand. *N. Z. J. Geol. Geophys.* 60, 497–518.
- VanTongeren, J.A., Kelemen, P.B., Hanghøj, K., 2008. Cooling rates in the lower crust of the Oman ophiolite: Ca in olivine, revisited. *Earth Planet. Sci. Lett.* 267, 69–82. <https://doi.org/10.1016/j.epsl.2007.11.034>.
- Velde, B., Hillier, S., 1991. Octahedral occupancy and the chemical composition of diagenetic (low-temperature) chlorites. *Clay Miner.* 26, 149–168.
- Vogel, W., Kuipers, G., 1987. A pre-calibrated program for geological applications. *Phillips New Developments in X-Ray Spectrometry*. vol. 11, pp. 2–8.
- Von Damm, K.L., 1995. Controls on the chemistry and temporal variability of seafloor hydrothermal fluids. *Seafloor Hydrothermal Systems: Physical, Chemical, Biological, and Geological Interactions*, pp. 222–247.
- Von Damm, K.L., Bischoff, J.L., Rosenbauer, R.J., 1991. Quartz solubility in hydrothermal seawater; an experimental study and equation describing quartz solubility for up to 0.5 M NaCl solutions. *Am. J. Sci.* 291, 977–1007.
- Warren, C.J., Parrish, R.R., Waters, D.J., Searle, M.P., 2005. Dating the geologic history of Oman's Samail ophiolite: insights from U-Pb geochronology. *Contrib. Mineral. Petrol.* 150, 403–422. <https://doi.org/10.1007/s00410-005-0028-5>.
- Warren, C.J., Searle, M.P., Parrish, R.R., Waters, D.J., 2007. Reply to Comment by F. Boudier and A. Nicolas on “dating the geologic history of Oman's Samail Ophiolite: Insights from U-Pb geochronology” by C.J. Warren, R.R. Parrish, M.P. Searle and D.J. Waters. *Contributions to Mineralogy and Petrology* vol. 154, 115–118. doi:<https://doi.org/10.1007/s00410-007-0182-z>
- Weyhenmeyer, C.E., 2000. Origin and Evolution of Groundwater in the Alluvial Aquifer of the Eastern Batinah Coastal Plain, Sultanate of Oman. PhD. University of Bern, Switzerland.
- White, W.M., Hofmann, A.W., Puchelt, H., 1987. Isotope geochemistry of Pacific Mid-Ocean Ridge Basalt. *J. Geophys. Res.* 92, 4881. <https://doi.org/10.1029/JB092iB06p04881>.
- Xie, X., Byerly, G.R., Ferrell Jr., R.E., 1997. Ilb trioctahedral chlorite from the Barberton greenstone belt: crystal structure and rock composition constraints with implications to geothermometry. *Contrib. Mineral. Petrol.* 126, 275–291.
- Xie, Z., Walther, J. V., 1993. Wollastonite + quartz solubility in supercritical NaCl aqueous solutions. *Am. J. Sci.* 293, 235.